NONLINEAR MR MODEL INVERSION FOR SEMI-ACTIVE CONTROL ENHANCEMENT WITH OPEN-LOOP FORCE COMPENSATION

by

Daniel Martin Reader

Thesis submitted to the faculty of the

Virginia Polytechnic Institute and State University

in partial fulfillment of the requirements for the degree of

Master of Science

In

Mechanical Engineering

Dr. Steve C. Southward, Chair

Dr. Mehdi Ahmadian

Dr. Saied Taheri

April 27, 2009
Danville, VA

Keywords: Magneto-Rheological Damper, Skyhook, Control, Inverse MR Damper

NONLINEAR MR MODEL INVERSION FOR SEMI-ACTIVE CONTROL ENHANCEMENT WITH OPEN-LOOP FORCE COMPENSATION

by

Daniel Martin Reader

(ABSTRACT)

The increased prevalence of semi-active control systems is largely due to the emergence of cost effective commercially available controllable damper technology such as Magneto-Rheological (MR) devices. Unfortunately, MR dampers exhibit highly nonlinear behavior, thus presenting an often over-looked complexity to the control system designer. With regards to controlling dampers, the well-known *Skyhook Damping* control algorithm has enjoyed great success for both fully active and semi-active control problems. The Skyhook design strategy is to create a control force that emulates what a passive linear damper would create when connected to an inertial reference frame. Skyhook control is device independent since it generates a desired control force command output that must be produced by the control system.

For simplicity, MR dampers are often assumed to have a linear relationship between the current input and the force output at a given relative velocity. Often this assumption is made implicitly and without knowledge of the underlying nonlinearity. This thesis shows that the overall performance of a semi-active Skyhook control system can be improved by explicitly inverting the nonlinear relationship between input current and output force. The proposed modification will work with any semi-active control algorithm, such as Skyhook, to insure that the controller performance is at least as good as the performance without the proposed modification. This technique is demonstrated through simulation on a quarter-vehicle system.

Hysteretic damping effects are incorporated into the modification by application of simple open loop force compensation. Laboratory testing of the hysteretic inversion process was performed with the goal of emulating an ideal linear damper without hysteresis. These results are compared with the implicit assumption thus providing a basis for validating the benefits of the improved methodology.

Acknowledgments

I would like to thank my advisor Dr. Steve Southward for his guidance and encouragement throughout my time as a Master's student. I would also like to thank Dr. Mehdi Ahmadian and Dr. Saied Taheri for serving on my committee.

I would also like to thank Mike Alex, Chandler Reubush, Bryan Pittman and Chris Boggs for their assistance and contributions in the testing phases of my research. Their individual areas of expertise were invaluable.

Finally, I would like to thank the ARC in conjunction with the Army/TARDEC for sponsoring my research.

Table of Contents

List of Figures

List of Tables

Chapter 1. Introduction and Literature Review

This chapter provides an introduction and overview for the research presented in this thesis. Existing literature on the subject areas covered in this thesis are presented.

1.1: Introduction

Magnetorhological (MR) dampers provide a platform for cost effective solutions for motion control applications. This is due to their relative simplicity, high force capability and low power consumption. Within the realm of automobiles, the MR damper has become an ideal actuator for generating controllable damping forces within primary and secondary suspension systems. As a result, their existence has motivated the development of a large number of control solutions. These solutions include semi-active sliding mode observers and controllers [4], adaptive semi-active (SA) controllers [5], and intelligent neural network-based controllers [13]. Chronologically, the very first control algorithm for governing the behavior a semi-active element was developed before the MR damper was readily available. This now well-known solution is called the Skyhook Damping control algorithm [8] and is used as used as a platform for further control development in this thesis.

1.1.1: Motivation

Due primarily to their semi-active nature, MR dampers provide an excellent platform for SA control. It can easily observed that the SA property of this category of damper is dependent upon the relative velocity across the damper itself. With the assumption of relative velocity being an uncontrollable input to the system, the non-passive magnitude of the damping force is then dependent solely upon current. Knowledge of these two signals allows for a map of the instantaneous force that the damper can generate.

While the highly nonlinear variable damping characteristics of MR devices have been widely analyzed [1,2,11,13,14], there has yet to be a study addressing the fundamental disconnect between the common, force-commanding SA control algorithms [2,7,10,11] and the current-controlled MR damper. To circumvent this disconnect, it became obvious that it was first necessary to understand the constitutive relationship between relative velocity and current input to the force output. Thus, a generalized separable model of the MR damper constitutive

relationship was needed. A method to explicitly invert this separable model was subsequently sought. Inversion of the current dependent component was used to determine the appropriate current for matching the MR damper force output to its commanded force.

1.1.2: Objectives

In short, the goal of this study was to develop a method to improve SA control law performance through bridging the gap between existing control solutions and the nonlinear dynamics of the SA actuator. Development of a forward model structure that allowed for mathematical inversion was the first objective. Successful validation of the forward model led toward the next objective of ensuring the forward model's invertibility. The final objective of this study was to implement the two models in a SA control simulation and validate the claims of improvement postulated by this thesis.

1.1.3: Outline

This section provides a brief view of the content of this work. Chapter two outlines the existing empirical MR damper model. The proposed separable model is then developed and validated. Chapter three overviews another approach analyzed for damper modeling. While this method was ultimately abandoned, concepts developed and restrictions observed were carried through to completion of this study. Chapter four describes the proposed empirical modeling procedure. Chapter five develops the inverse of the empirical model. The rules for performing this step are formulated and the model is validated. Chapter six introduces the effects of modeled hysteresis into the proposed forward and inverse models. A method for tuning the effects of modeled hysteresis is then detailed. Chapter seven incorporates the inverse model from Chapter five into a semi-active control law. Chapter eight applies the improved semi-active control law into a simulation study. The results of this simulation are then discussed. This thesis then concludes with an evaluation of the work and recommendations for further development.

1.2: Damper Characterization

Accurate representation of any modeled element will improve simulation results and ease control algorithm development. With MR dampers being of interest in this study, a method to characterize the dampers for use in both simulation and real world instances has been developed. In the ideal characterization environment, damper force and velocity would be measured within

the system the damper is implemented [15]. However, more often than not, this is not practical due to costs, packaging, etc. Fortunately, test systems such as the Roehrig EMA Shock Dynamometer and Roehrig Shock software exist for this very purpose [3].

With regards to the instrumentation used in raw characterization data collection, the shock dynamometer records displacement, force and temperature while exciting the system with a sinusoid [16]. From this batch of sampled data, the displacement is differentiated to produce velocity data. As a result, the dampers ability to generate force can be observed with respect to both position, Figure 1.1b and velocity, Figure 1.1a.

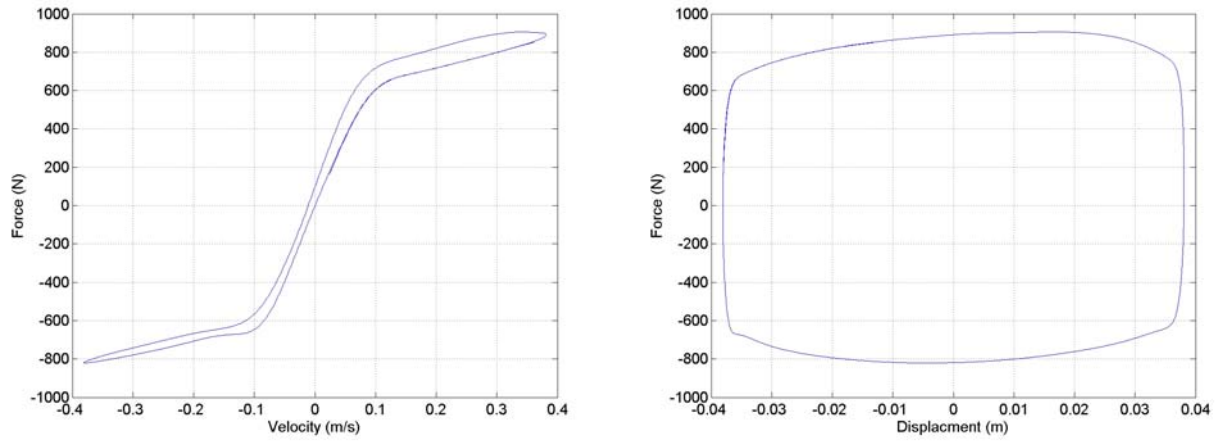

(a) (b)

Figure 1.1. Generic characterization data: (a) force-velocity and (b) force-displacement.

In the testing of MR dampers, the standard test procedure outlined by Dixon is followed [16], but is augmented by means of application of a DC current. The characterization process is then performed multiple times to collect data at the desired DC current levels [17]. For comparison, Figure 1.1 displays generic results of a standard damper characterization process while Figure 1.2 presents the force-velocity curves associated with a MR damper.

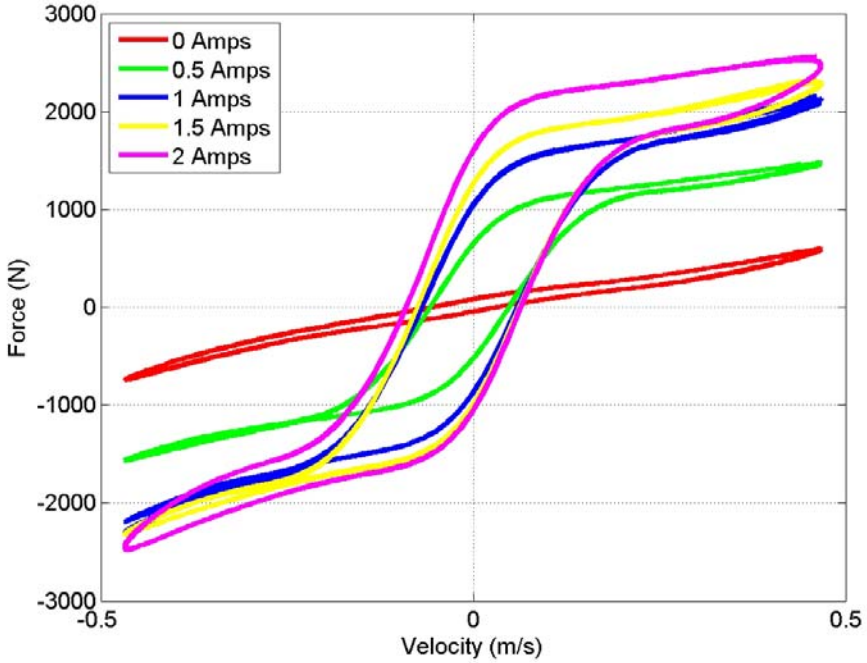

Figure 1.2. Force-velocity traces for currents ranging from 0 to 2 amps. Test specimen is a Lord RD-1005-3 MR damper.

1.3: Damper Models

Modeling the behavior of the MR damper has been a thoroughly analyzed topic. While this area has been studied by many researchers who have each formulated their own models, for brevity, this section will focus on a select few works which have become commonplace throughout the field. This section will outline the pertinent existing art in this area and conclude with justification for development of the proposed model.

1.3.1: Parametric Model

As proposed by both Wen and Spencer, the MR damper can be modeled parametrically. This parametric modeling structure characterizes the MR damper as a system comprised of nonlinear mechanical elements such as springs and dampers [18, 17]. Spencer's model, the most common state-of-the-art parametric model, expanded upon the preexisting model developed by Wen [18, 19]. Also known as the Bouc-Wen model, shown in Figure 1.3a, this early model describes MR damper force as

$$F = c_0 \dot{x} + k_0 \left(x - x_0 \right) + \alpha z \,. \tag{1.1}$$

A Markov-vector representation is implemented for modeling the nonlinear hysteretic portion of the system. Its evolutionary state z is governed by

$$\dot{z} = -\gamma\left|\dot{x}\right|z\left|z\right|^{n-1} - \beta\dot{x}\left|z\right|^{n} + A\dot{x}\,. \tag{1.2}$$

As depicted in Figure 1.3b, Spencer et. al., first added a series resistance to the Bouc-Wen model. A compliance was then placed in parallel to that system thus producing their model predicting the MR damper force

$$\begin{cases} \dot{z} = -\gamma\left|\dot{x}-\dot{y}\right|z\left|z\right|^{n-1} - \beta\left(\dot{x}-\dot{y}\right)\left|z\right|^{n} + A\left(\dot{x}-\dot{y}\right) \\ \dot{y} = \dfrac{1}{c_0+c_1}\left\{\alpha z + c_0\dot{x} + k_0\left(x-y\right)\right\} \\ F_{MR} = c_1\dot{y} + k_1\left(x-x_0\right) \end{cases}, \tag{1.3}$$

where z is an evolutionary state and y is the intermediate displacement.

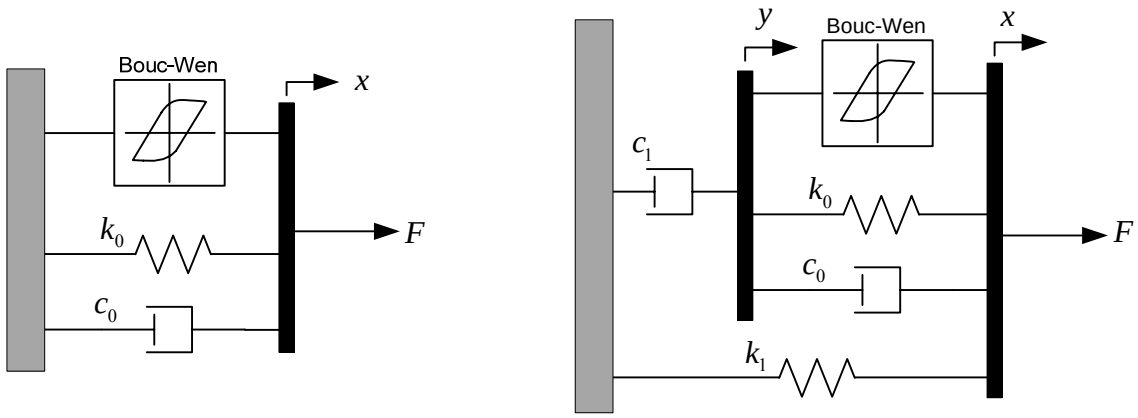

(a) (b)

Figure 1.3. Graphical representation of the Bouc-Wen parametric MR damper model (a) and the Spencer model (b).

Further details regarding the constants used in equations 1.1 to 1.3 are presented in the literature [19, 18, 17].

As noted by Song [17], these models generally provide a good characterization of the dynamics of the damper but they can be quite hard to solve numerically. This notion of numerical inefficiency is further supported by Jun, et. al. [20]. In this work the authors depart from the Spencer model and develop a Blackbox model for the MR damper. They go on to note that

singularities in the evolutionary state variable require a high integration step rate (KHz range) to maintain numerical stability, thus increasing computational cost in real-time applications. This study also states that performing the parameter optimization necessary to complete this model is a delicate task as the highly nonlinear structure requires advanced search algorithms and carefully selected initial conditions. Based on these issues underlying the existing parametric forward model, the proposed task of development of an inverse model would further compound these existing computational shortcomings.

1.3.2: Non-parametric Model

As presented by Song [17], an alternate to the parametric method of modeling MR dampers is the non-parametric method. Using this approach, the device is represented through purely empirical expressions. Included are the experimental force characteristics of the MR damper, equations capturing various shapes and trends, and an optimization routine fitting these equations to characterization data.

From observation of characterization data, the term *backbone* is defined as the underlying function governing the overall non-hysteretic shape of the force-velocity data. Thus, a derivative of the hyperbolic tangent function can be used to generalize this behavior [17]

$$S_b(V) = \frac{\left(b_0 + b_1\left|V - V_0\right|\right)^{b_2(V-V_0)} + \left(b_0 + b_1\left|V - V_0\right|\right)^{-b_2(V-V_0)}}{b_0^{b_2(V-V_0)} + b_0^{-b_2(V-V_0)}}. \tag{1.4}$$

Further, plotting the current versus maximum damping force depicts the effects of magnetic saturation occurring at high currents. From this data, a polynomial curve fit is proposed

$$A_{MR}(I) = \sum_{i=0}^{n} a_i I^i. \tag{1.5}$$

Finally, the presence of hysteresis is accounted for using a first order filter. The coefficients of this filter are adjusted with regards to the current level thus providing a good fit throughout the entire range. This filter is described here in a state-space formulation

$$\dot{x} = -\left(h_0 + h_1 I + h_2 I^2\right)x + h_3 F_s, \tag{1.6a}$$

$$F_h = \left(h_0 + h_1 I + h_2 I^2\right)x + h_4 F_s. \tag{1.6b}$$

The parameter optimization algorithm can then be defined with the following cost function

$$J = \sum_{k=1}^{N} \left[F_{mr}(k) - F_{ex}(k) \right]^2 \tag{1.7}$$

where F_{ex} is the experimentally measured force from characterization data.

Computationally, this approach outperforms the parametric model [17]. Also, its invertibility is dependent upon equation (1.5) governing the curve fit. The non-parametric structure of this model provides a platform for further model development with the ultimate goal of rapid model inversion.

1.4: MR Damper Model Inversion

As suggested by Zhou et. al., inverse dynamic compensation is an intuitive way to linearize hysteresis behavior [26]. Their study presents a closed-loop control method used to reduce force error with the goal of linear damping characteristics. By building inverse models based on the Bingham Model [27], their proposed Modified Bingham Model and the Bouc-Wen model [18, 19], the authors performed a control study to evaluate performance. Consequently, the internal dynamics of the Bouc-Wen model made accurate inversion nearly impossible and highly inefficient. Ultimately, their inversion study focused on their proposed Modified Bingham Model. While the work presents a viable option for hysteretic compensation, the added cost of the series load cell required for closing the loop renders their solution less attractive.

1.5: Semi-Active Control

While semi-active control algorithms have been thoroughly analyzed and studied in the literature [2, 7, 10, 11], there has not been any study that addresses a common pitfall associated with semi-active control design using dissipative controllable devices such as MR dampers. In particular, control algorithms are developed and applied to MR devices without explicitly considering the physical semi-active nature of the device. However, the original Skyhook control algorithm [8] explicitly takes into consideration device implementation by insuring that the algorithm only commands dissipative forces. Many control algorithms are derived with a control force command that is simply applied to the MR damper. The sole conversion between force-command and current-command is borne out of the implicit assumption that the MR damper force is proportional to the applied current. As will be shown, experimental characterization data

demonstrates how this assumption can sometimes produce reasonable results; however, as will also be shown, it is generally not a good assumption.

Chapter 2. Separable Damper Model

For the most part, passive dampers are nonlinear devices; however, Magneto-Rheological (MR) fluid dampers possess an additional degree of nonlinear complexity due to the external input, typically a controlled current. In its off state, the damper exhibits standard passive damping behavior, but the application of current magnifies the range of available damping forces. Many mathematical models have been developed to capture this nonlinear behavior [1, 14]. For development of a new separable damper model, existing nonlinear MR damper models which produce a force output due to relative velocity and the control current inputs will be used as a basic structure.

2.1: Simple Empirical MR Damper Model

Highly complex phenomenological models, such as the Spencer model [1] are useful for understanding and improving the device design, but they tend to be somewhat impractical for control system development. Possibly the simplest empirical model of nonlinear MR constitutive behavior is the following

$$F_{MR}^{simple}\left(i, v_{rel}\right) = \underbrace{\left[\lambda\ abs\left(i\right)\right]}_{\substack{\text{Current}\\ \text{Dependence}}} \times \underbrace{\left[\text{sgn}\left(v_{rel}\right)\right]}_{\substack{\text{Velocity}\\ \text{Dependence}}}, \tag{2.1}$$

where λ is a constant that relates the applied current (i) to the force output (F_{MR}) ,[28]. Notice from equation (2.1) that the damper behaves exactly the same for both positive and negative currents. Also notice that this model is separable, i.e., the current dependent term is completely independent of the velocity dependent term. Since only the sign of the velocity (v_{rel}) is used in this model, the velocity dependence is functionally present to enforce a first-and-third quadrant or "dissipative" constitutive relationship.

The structure of the simple MR damper model in equation (2.1) is motivated by experimental characterizations of a class of actual MR devices such as Lord Rheonetic dampers [2]. Clearly, not all MR dampers behave the same; however, many MR devices can roughly be described by equation (2.1) and produce experimental characterization data similar to that shown in Figure 2.1 below. During a typical characterization process, the output force due to a sinusoidal relative velocity excitation is plotted at a series of constant current inputs.

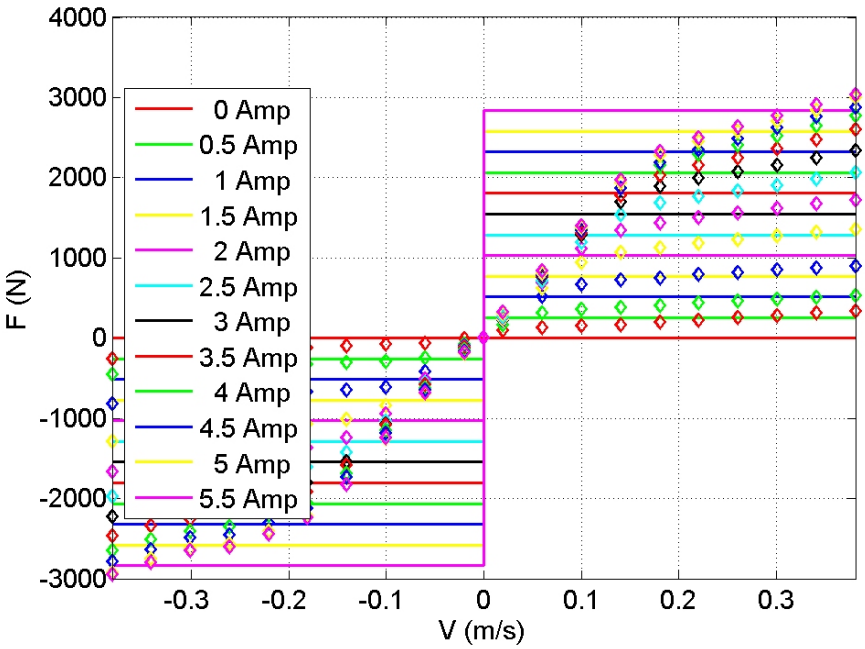

Figure 2.1. Comparison of output force from the simple MR damper model of equation (2.1.1) for λ=600 with typical experimental characterization data of a MagnaRide damper (marked with ◊) for a sinusoidal relative velocity input at constant currents.

Most real dampers, passive or otherwise, exhibit hysteresis due to some form of series compliance in the device. Evidence of hysteresis is clearly absent from the experimental characterization data of Figure 2.1. This is because the test equipment typically used to measure this characterization data, such as a Roehrig EMA Shock Dynamometer [3], shown with a MagnaRide damper in Figure 2.2, performs averaging on the raw force vs. velocity data to effectively remove the hysteresis, leaving only the *backbone* curves that are shown in Figure 2.1. Although hysteresis is an important aspect of the dynamic response, the basis for modeling will be restricted to models for the "static" or *backbone* constitutive relationship. Hysteretic extensions to this formulation will be presented in a later chapter.

Although the simple MR damper model does predict the gross constitutive trends in the data, it is generally not adequate for high performance control systems or for high fidelity simulations largely because of the errors induced at relatively low velocities, and because the force-to-current dependence deviates from linearity due to magnetic field saturation in the coil.

Figure 2.2. Laboratory setup for experimental characterization of the MR damper.

2.2: Proposed Separable MR Damper Model

Motivated by the conventional characterization data for an MR damper as indicated in Figure 2.1, and building upon the simple model in equation (2.1.1), we generalize the separable terms to formulate a new nonlinear empirical MR damper model

$$F_{MR}(i,v) = [f(i)] \times [g(v_{rel})], \tag{2.2}$$

where the current dependent term $f(i)$ is only defined for positive currents $i \in [0, i_{\max}]$, and the velocity dependent term $g(v_{rel})$ is a first-and-third quadrant nonlinear function. We impose the

restriction that $f(i)$ be positive and monotonic, and the condition $f(0) > 0$ represents the common practical situation where every MR damper has a non-zero "off" state. We also impose the restriction that $g(v_{rel})$ is monotonic and $g(0) = 0$, but anticipate that $g(v_{rel})$ will not necessarily be symmetric. When using this model (2.2) in simulation or for real-time, both $f(i)$ and $g(v_{rel})$ may be implemented as an interpolated table-look-up or approximated with polynomials or any other suitable function. Note also that $f(i)$ has units of force, whereas $g(v_{rel})$ is non-dimensional.

Chapter 3. Volterra Representation

3.1: Overview

As stated in Section 2.2, the separable function, equation (2.2), describing the nonlinear empirical MR damper model can be implemented through table-look-ups, approximate polynomials, or any other suitable function. A Volterra filter was initially proposed as a method for approximating the MR damper model. In addition to its abilities to incorporate a wide range of dynamic effects and nonlinearities, the proposed Volterra filter became attractive for its ability to be implemented in an adaptive form potentially allowing for on-line system identification.

The formal Volterra series expansion can be viewed as a general Taylor series expansion upon a function with memory [21]

$$\begin{aligned} y(n) = h_0 + \sum_{i=0}^{\infty} h_1(i)\,x(n-i) + \sum_{i=0}^{\infty}\sum_{j=0}^{\infty} h_2(i,j)\,x(n-i)\,x(n-j) \\ + \sum_{i=0}^{\infty}\sum_{j=0}^{\infty}\sum_{k=0}^{\infty} h_3(i,j,k)\,x(n-i)\,x(n-j)\,x(n-j) + \cdots \end{aligned}, \tag{3.1}$$

where $h_p(m_1, m_2, \ldots, m_p)$ is the p^{th}-order Volterra kernel. This series is shown in discrete time with the output, *y(n)*, and input sample, *x(n)*.

3.2: Development

For implementation in an adaptive signal processing scheme, the Volterra series was defined in terms of a filter [21]

$$\begin{aligned} y(n) = f_0 + \sum_{i=0}^{N-1} f_1(i)\,x(n-i) + \sum_{i=0}^{N-1}\sum_{j=0}^{N-1} f_2(i,j)\,x(n-i)\,x(n-j) \\ + \sum_{i=0}^{N-1}\sum_{j=0}^{N-1}\sum_{k=0}^{N-1} f_3(i,j,k)\,x(n-i)\,x(n-j)\,x(n-k) + \cdots \end{aligned}, \tag{3.2}$$

with memory span $N-1$, linear coefficient f_1, quadratic coefficient f_2, and k^{th}-order kernel coefficient f_k.

Building on the assumption of a *separability* developed in Chapter 2, the independent force and velocity terms were assigned their own Volterra series filters, equations (3.3 & 3.4). Assuming the existence of an optimal number of terms in each series, the finite series polynomial expansions became

$$g(v) = \beta_0 + \beta_1 v + \beta_2 v^2 + \cdots + \beta_M v^M , \tag{3.3}$$

$$f(i) = \alpha_0 + \alpha_1 i + \alpha_2 i^2 + \cdots + \alpha_N i^N . \tag{3.4}$$

Independent reduction of these two expressions, equations (3.3) and (3.4), defined the vector notation of the coefficients and variables:

$$\mathbf{b} = \begin{bmatrix} \beta_0 & \beta_1 & \beta_2 & \cdots & \beta_M \end{bmatrix}, \tag{3.5}$$

$$\mathbf{v} = \begin{bmatrix} 1 & v & v^2 & \cdots & v^M \end{bmatrix}, \tag{3.6}$$

$$\mathbf{a} = \begin{bmatrix} \alpha_0 & \alpha_1 & \alpha_2 & \cdots & \alpha_N \end{bmatrix}, \tag{3.7}$$

$$\mathbf{i} = \begin{bmatrix} 1 & i & i^2 & \cdots & i^N \end{bmatrix}, \tag{3.8}$$

which could be compactly expressed as

$$g(v) = \mathbf{v}\mathbf{b}^T = \mathbf{b}\mathbf{v}^T , \tag{3.9}$$

and

$$f(i) = \mathbf{i}\mathbf{a}^T = \mathbf{a}\mathbf{i}^T . \tag{3.10}$$

Combining these terms in the form of equation (2.2) produced the following vector-matrix representations of the MR damper.

$$\begin{aligned} F_{MR}(i,v) &= g(v)\, f(i) \\ &= \mathbf{b}\left[\mathbf{v}^T\mathbf{i}\right]\mathbf{a}^T \\ &= \begin{bmatrix} \beta_0 & \beta_1 & \cdots & \beta_M \end{bmatrix} \begin{bmatrix} 1 & i & \cdots & i^N \\ v & vi & & vi^N \\ \vdots & & \ddots & \vdots \\ v^M & vi^M & \cdots & v^M i^N \end{bmatrix} \begin{bmatrix} \alpha_0 \\ \alpha_1 \\ \vdots \\ \alpha_N \end{bmatrix} \end{aligned} \tag{3.11}$$

$$
\begin{aligned}
F_{MR}(i,v) &= g(v)\, f(i) \\
&= \mathbf{v}\left[\mathbf{b}^T\mathbf{a}\right]\mathbf{i}^T \\
&= \begin{bmatrix} 1 & v & v^2 & \cdots & v^M \end{bmatrix}
\begin{bmatrix} \beta_0\alpha_0 & \beta_0\alpha_1 & \cdots & \beta_0\alpha_N \\ \beta_1\alpha_0 & \beta_1\alpha_1 & & \beta_1\alpha_N \\ \vdots & & \ddots & \vdots \\ \beta_M\alpha_0 & \beta_M\alpha_1 & \cdots & \beta_M\alpha_N \end{bmatrix}
\begin{bmatrix} 1 \\ i \\ i^2 \\ \vdots \\ i^N \end{bmatrix}
\end{aligned} \tag{3.12}
$$

As shown in equations (3.11 & 3.12), there exists a certain degree of ambiguity in the order that vectors are multiplied, thus there are two possible forms depicting the interactions of the filter coefficients and variables. However, in their present form, neither representation has practical functionality. To address this, a reshaping scheme was devised. This scheme consisted of stacking the matrices from each method row-wise, thus creating the input and weight vectors of equation (3.13) and equation (3.14), respectively.

$$
\mathbf{v}^T\mathbf{i} = \begin{bmatrix} 1 & i & \cdots & i^N \\ v & vi & & vi^N \\ \vdots & & \ddots & \vdots \\ v^M & vi^M & \cdots & v^M i^N \end{bmatrix}
\quad \Rightarrow \quad
\begin{bmatrix} 1 \\ v \\ \vdots \\ v^M \\ \vdots \\ i^N \\ vi^N \\ \vdots \\ v^M i^N \end{bmatrix} \equiv \mathbf{X} \tag{3.13}
$$

$$
\mathbf{a}^T\mathbf{b} = \begin{bmatrix} \alpha_0\beta_0 & \alpha_0\beta_1 & \cdots & \alpha_0\beta_M \\ \alpha_1\beta_0 & \alpha_1\beta_1 & & \alpha_1\beta_M \\ \vdots & & \ddots & \vdots \\ \alpha_N\beta_0 & \alpha_N\beta_1 & \cdots & \alpha_N\beta_M \end{bmatrix}
\Rightarrow
\begin{bmatrix} \beta_0\alpha_0 \\ \beta_1\alpha_0 \\ \vdots \\ \beta_M\alpha_0 \\ \vdots \\ \beta_0\alpha_N \\ \beta_1\alpha_N \\ \vdots \\ \beta_M\alpha_N \end{bmatrix}
=
\begin{bmatrix} w_0 \\ w_1 \\ \\ \\ \vdots \\ \\ \\ \vdots \\ w_{(N+1)(M+1)} \end{bmatrix} \equiv \mathbf{W} \tag{3.14}
$$

With this modification to the structure, the Volterra filter representation is transformed into a more familiar FIR-like [22] form described by equations (3.15a-b).

$$F_{MR}(i,v) = (\alpha_0\beta_0) + (\alpha_0\beta_1 v + \alpha_1\beta_0 i) + (\alpha_0\beta_2 v^2 + \alpha_1\beta_1 iv + \alpha_2\beta_0 i^2) + \cdots \tag{3.15a}$$

$$F_k(v_k,\ i_k) = \underbrace{w_0}_{\text{DC}} + \underbrace{w_1 i_k + w_2 v_k}_{\text{Linear}} + \underbrace{w_3 i_k^2 + w_4 v_k^2}_{\text{Quadratic}} + \underbrace{w_5 i_k v_k + w_6 v_k i_k^2 + w_7 i_k v_k^2}_{\text{Cross-product}} + \cdots \tag{3.15b}$$

$$F_k(i_k, v_k) = \mathbf{W}_k^T \mathbf{X}_k = \mathbf{X}_k^T \mathbf{W}_k \tag{3.15c}$$

Looking ahead, each value of in the coefficient vector, **W**, became capable of representing of an adjustable weight in an adaptive signal processing scheme.

3.3: Volterra MR Damper Model

To perform an adaptive modeling operation, a plant must first exist. Whether this plant is a physical object or a simulated element, the adaptive filter needs to have a target. With simulation being the most time efficient process for development, a Volterra model of the damper was implemented as the plant using the structure from equation (3.15c).

Using laboratory data including the current levels and peak forces generated, a curve governing force and current was approximated using a 3rd order polynomial curve fit shown in Figure 3.1. To capture the trend of the velocity *backbone*, a sigmoidal function was adopted

$$g(v) = \left(1 - e^{-\frac{|v|}{v_0}}\right) sign(v). \tag{3.16}$$

The shape generated by this function over the range of velocity interest is shown in Figure 3.2. This trend was then approximated using a 10th order polynomial curve fit.

Combining the information from the curve fits of the *g(v)* and *f(i)* data of Figures 3.1 and 3.2 into the equation (3.15a) yielded the Volterra-based MR damper model shown in Figure 3.3. Comparison of Figures 3.3 and 3.4 shows how well the model mimics the actual damper.

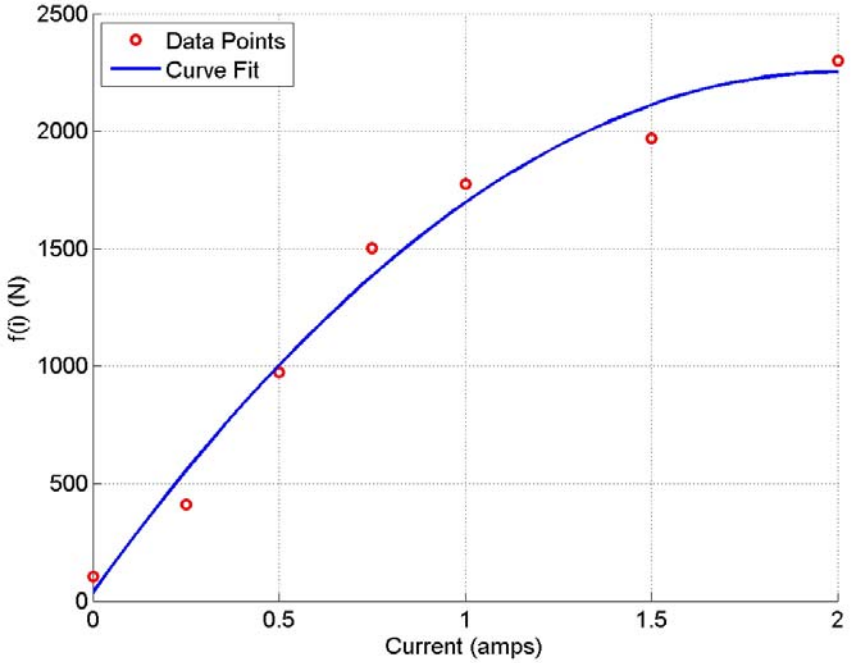

Figure 3.1. Current versus Force for a Lord RD-1005 damper showing the 3rd order curve fit to approximate the trends seen in the characterization data.

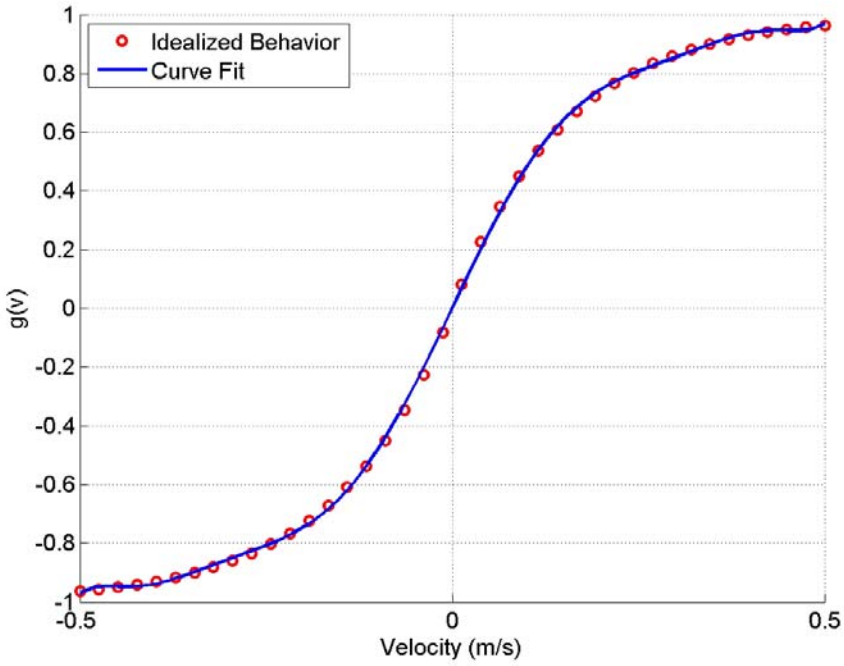

Figure 3.2. Velocity versus non-dimensional amplitude showing the 10th order curve fit used to approximate the trends seen in characterization data.

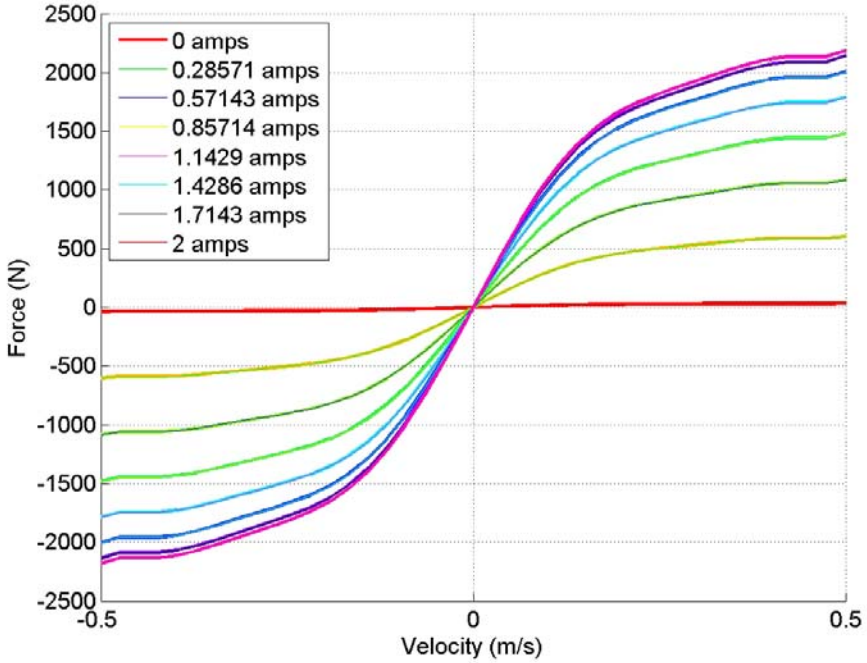

Figure 3.3. Force vs. velocity traces for currents ranging from 0 to 2 amps.

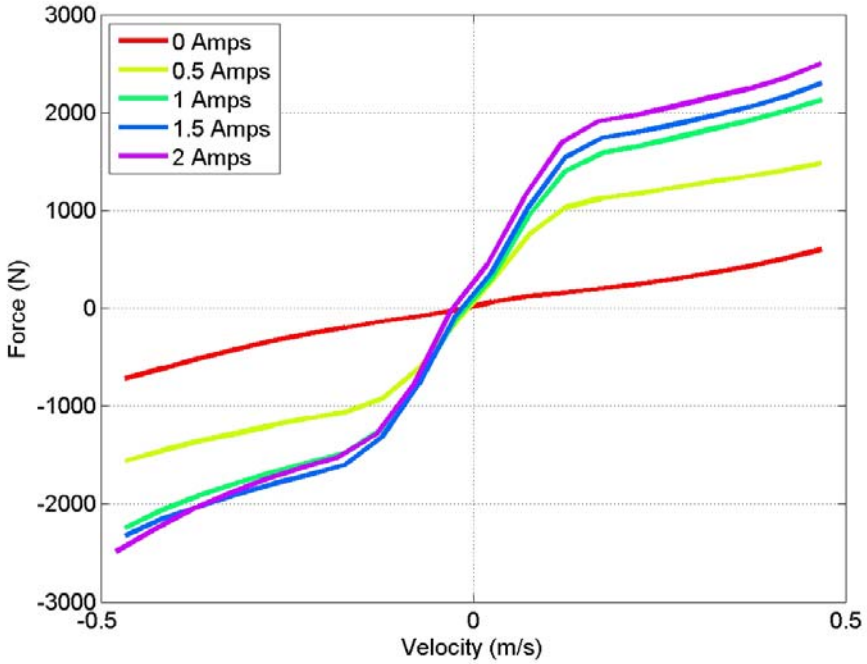

Figure 3.4. Actual Characterization data.

3.4: Adaptation Constraints:

In an effort to simplify the adaptation, a set of constraints were imposed based on observed physical behavior of the damper. From the Chapter 2 discussion regarding the separable model, both the current and velocity dependent terms had the capacity to be approximated by curve fits. Looking back to the data presented in Figures 3.1 and 3.2, curve fits representing the data sets with polynomials are shown.

Inspection of the current-dependent curve, Figure 3.1, led to three constraint conditions. First, it was observed that at zero current, the damper still produced a force, i.e. the damper became a purely passive device in its off state. Setting the current equal to zero in equation (3.4) and simplifying

$$\begin{aligned} f(0) &= \alpha_0 + \alpha_1(0) + \alpha_2(0)^2 + \cdots + \alpha_N(0)^N \\ f(0) &= f_0 = \alpha_0 \end{aligned} \tag{3.17}$$

where f_0 is defined as the force capacity at zero current generated the mathematical representation for this phenomena.

Next, it was noticed that the current-dependent curve increases monotonically. To ensure this general contour, the slope at zero current needed to be kept positive. This observation bore the necessity of keeping the first derivative positive.

$$\begin{aligned} & f'(0) > 0 \\ & \quad f'(i) = \alpha_1 + \alpha_2 i + 2\alpha_3 i^2 + \cdots + (N)\alpha_N i^{N-1} \\ & \quad f'(0) = \alpha_1 + \alpha_2 0 + 2\alpha_3 0^2 + \cdots + (N)\alpha_N 0^{N-1} > 0 \\ & \quad f'(0) = \alpha_1 > 0 \\ & \quad \therefore\ \alpha_1 > 0 \end{aligned} \tag{3.18}$$

Finally, to further capture the magnetic saturation behavior, the concave-down shape to the curve needed to be enforced. This was accomplished by ensuring that the second derivative was always negative.

$$
\begin{aligned}
&f''(i) < 0 \\
&\quad f(i) = \alpha_0 + \alpha_1 i + \alpha_2 i^2 + \alpha_3 i^3 + \cdots + \alpha_N i^N \\
&\quad f'(i) = 0 + \alpha_1 + 2\alpha_2 i + 3\alpha_3 i^2 + \cdots + (N)\alpha_N i^{N-1} \\
&\quad f''(i) = 2\alpha_2 + \cancel{6\alpha_3 i + \cdots + (N)\alpha_N i^{N-1}} < 0 \\
&\quad \therefore 2\alpha_2 < 0 \\
&\quad \alpha_2 < 0
\end{aligned}
\tag{3.19}
$$

Assessment of the generic velocity dependence curve from Figure 3.2 suggested two more obvious constraints. First, a true zero crossing was needed.

$$
\begin{aligned}
g(0) &= \beta_0 + \beta_1 0 + \beta_2 0^2 + \cdots + \beta_M 0^M = 0 \\
g(0) &= \beta_0 = 0 \\
\beta_0 &= 0
\end{aligned}
\tag{3.20}
$$

Next, a positive slope at zero was enforced.

$$
\begin{aligned}
g(v) &= \beta_0 + \beta_1 v + \beta_2 v^2 + \cdots + \beta_M v^M \\
g'(v) &= 0 + \beta_1 + 2\beta_2 v + \cdots + M\beta_M v^{M-1} \\
g'(0) &= \beta_1 \quad \Rightarrow \quad \beta_1 > 0
\end{aligned}
\tag{3.21}
$$

With these five constraints, it became possible to simplify the pending adaptation step to help steer the algorithm form exploring in unnecessary directions. Examples of these constraints applied to a system are shown in Appendix B.

3.5: Volterra Parameter Adaptation:

Again, the goal of the parameter adaptation simulation was to identify the unknown coefficients of the Volterra MR damper model. To implement this, a simulation using the LMS [23] gradient search algorithm was constructed.

$$
\mathbf{W}_{k+1} = \mathbf{W}_k + \mu \varepsilon_k \mathbf{X}_k \tag{3.22}
$$

Using Simulink, the block diagram of Figure 3.5 was constructed. This system operated upon discrete velocity and current data, assumed to be band-limited white-noise, and generated an error signal. Each subsystem used its own algorithm for producing damper force. The *Volterra-Modeled MR Damper* block implemented equation (3.15a) with known coefficients based on the

data of Figures 3.1 to 3.3, while the *Adaptive Volterra Filter* block implemented the LMS algorithm, equation (3.22) and Figure 3.6, along with equation (3.15c). Along with the constraints defined in section 3.4, the initial conditions of the filter were set within 10% of their true values to ease the adaptation.

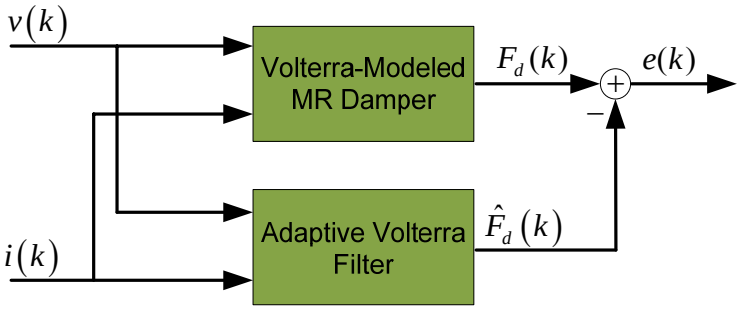

Figure 3.5. Block diagram for the parameter estimation simulation.

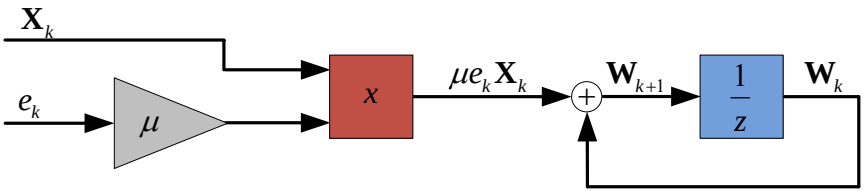

Figure 3.6. Block diagram for LMS updating algorithm embedded within the Adaptive Volterra Filter block of Figure 3.4.

Simulation was run for a total of 250 seconds and the adaptation was turned on at 125 seconds. Force error was then calculated and used to describe the performance of the adaptive algorithm.

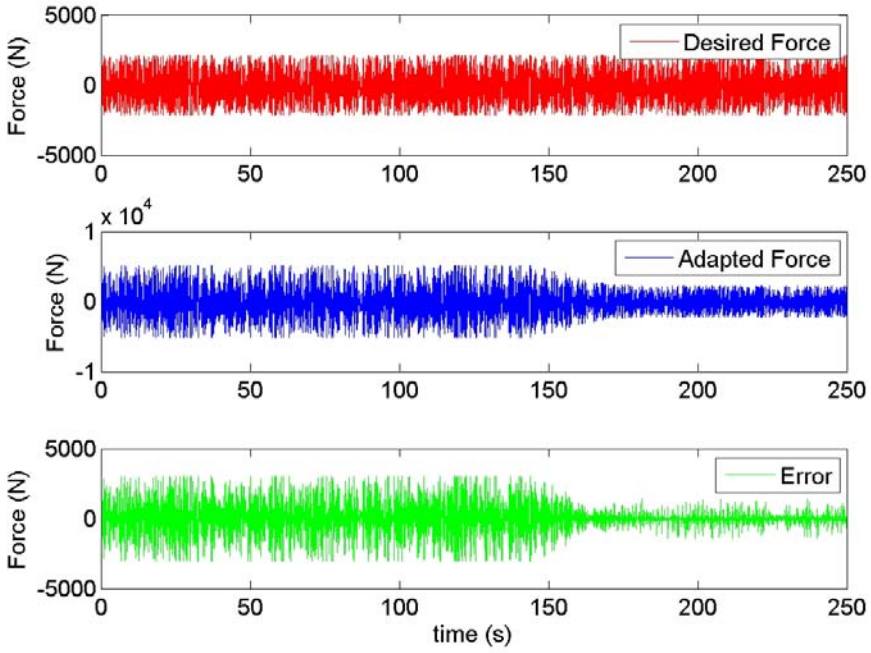

Figure 3.7. Force error from adaptation simulation.

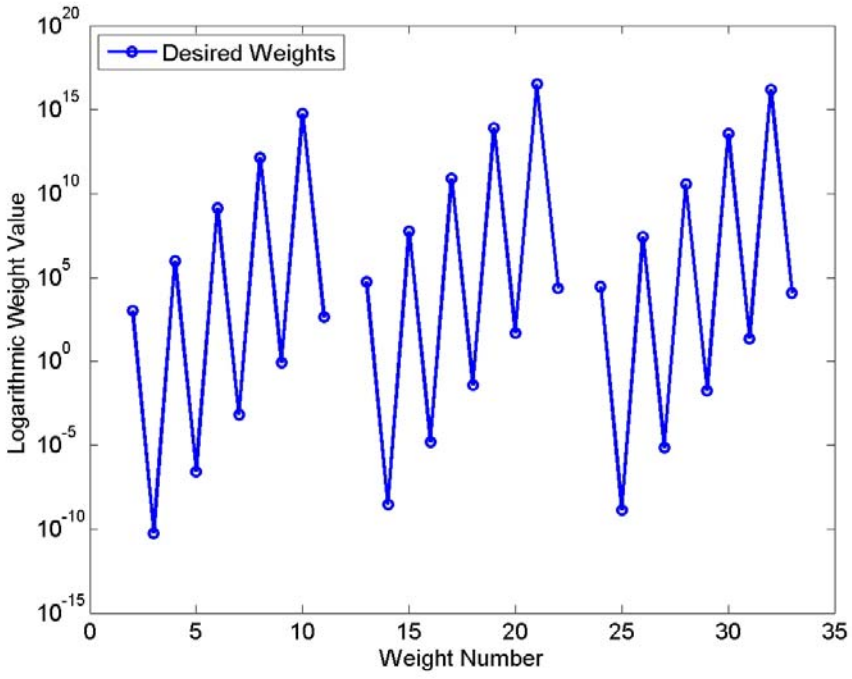

Figure 3.8. True weight distribution showing the scale that the LMS algorithm must cover to find a solution.

Due to the information from figure 3.7 showing that the simulation never fully converges, it is clear that the solution space is not convex as there exist multiple local minima. In addition, the

range in which the desired weights exist approaches 30 orders of magnitude as shown in Figure 3.8. With the failure of the adaptive algorithm to successfully converge, it was presumed that reformulating the simulation to adapt on an inverse was not worth pursuit.

The problems experienced here could be potentially overcome by using a random search method such as Simulated Annealing or a Genetic Search algorithm, but for this thesis, this method will be abandoned for the empirical methods subsequently developed in this work.

Chapter 4. Empirical Modeling Procedure

As the Volterra adaptation failed to converge, a new method of modeling the damper was proposed. This method relied purely upon data gathered from the characterization process described above. Direct implementation of this observed, or empirical, data provided the best representation of the damper behavior.

The two separable functions f and g in equation (2.2) may be numerically estimated from conventional characterization data such as that shown in Figure 2.1. The first step in the estimation process is to divide all of the force vs. relative velocity data for a given current by the corresponding data for some nominally chosen current. For example, the data associated with a mid-range nominal current such as 1 Amp could be used as a representative data set for the normalization.

$$\alpha(i, v_{rel}) = \left(\frac{F_{MR}(i, v_{rel})}{F_{MR}(i_{\text{nominal}}, v_{rel})} \right) \quad \forall i \tag{4.1}$$

Figure 4.1a indicates that the scale factor α defined by (2.2) is roughly constant for each current. Notice from Figure 4.1 that the zero-velocity data has been omitted from the computation so as to avoid a zero-divide condition. The next step is to scale all of the original MR damper force data $F_{MR}(i, v_{rel})$ by the average value of the α scale factor for each current,

$$F_{scaled}(i, v_{rel}) = \left(\frac{F_{MR}(i, v_{rel})}{\overline{\alpha(i)}} \right), \tag{4.2}$$

where $\overline{\alpha(i)}$ is averaged across all velocity data for a given current. By using an average value of α, all of the data associated with non-zero velocity will contribute to the final estimate. The result of this step is shown in Figure 4.1b where we see that all of the scaled force data resides in the vicinity of the force data associated with the selected nominal current. Because of this, we are now able to average the force data across current at each velocity point to estimate an average scaled force $\overline{F_{scaled}(v_{rel})}$. The average scaled force is plotted as a black solid line in Figure 4.1b.

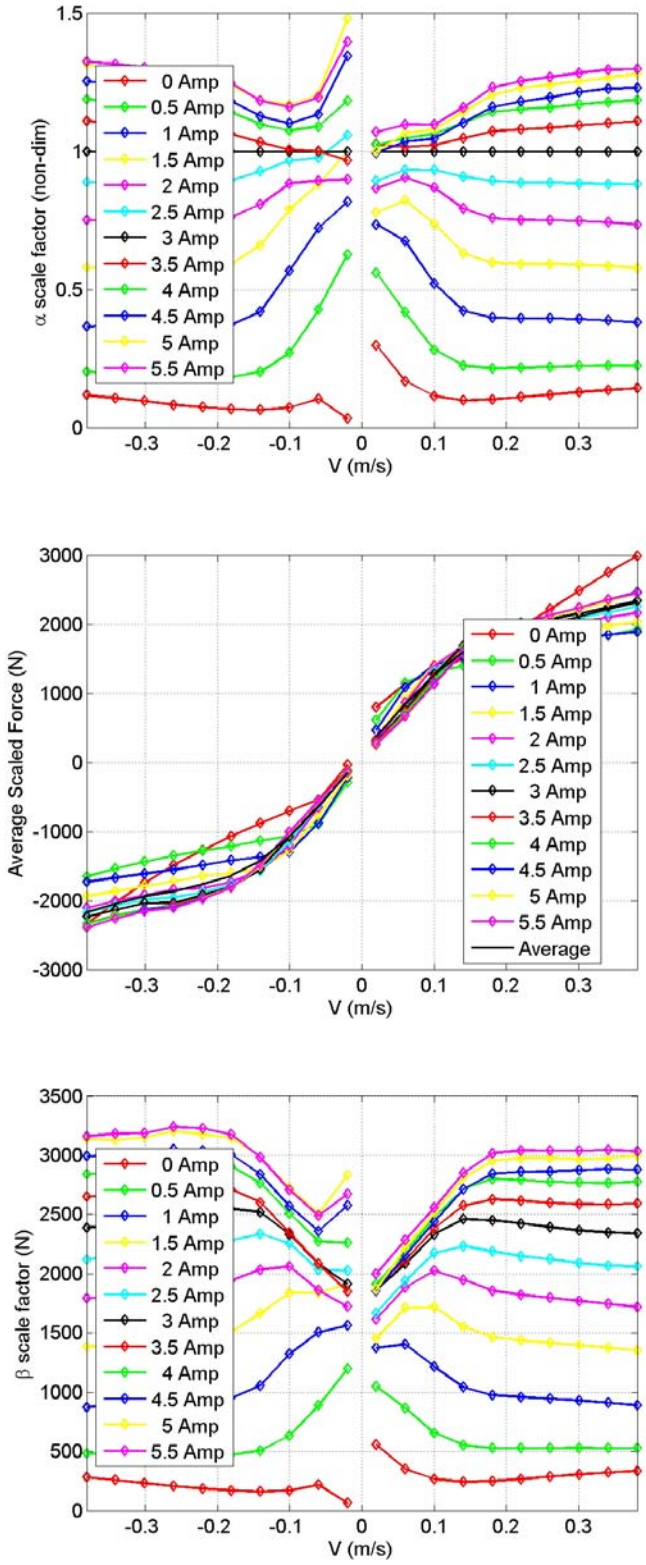

Figure 4.1. Intermediate steps in the estimation process for the separable MR damper model: (a) individual α scale factor data, (b) average scaled force data, (c) individual β scale factor data.

The average scaled force is essentially the average velocity dependent term. From the definition above in equation (2.2), this factor is non-dimensional, therefore we must divide by the maximum absolute value of the average scaled force to obtain the empirical estimate for $g(v_{rel})$

$$g(v_{rel}) = \left(\frac{\overline{F_{scaled}(v_{rel})}}{\max\left|\overline{F_{scaled}(v_{rel})}\right|} \right). \tag{4.3}$$

Figure 4.2 is a plot of the result for the numerically estimated velocity dependent term $g(v_{rel})$ using equation (2.2). Notice that this data clearly meets the requirement that $g(v_{rel})$ be a 1st & 3rd quadrant nonlinearity. The condition that $g(0) = 0$ is strictly enforced by simply setting the value to zero.

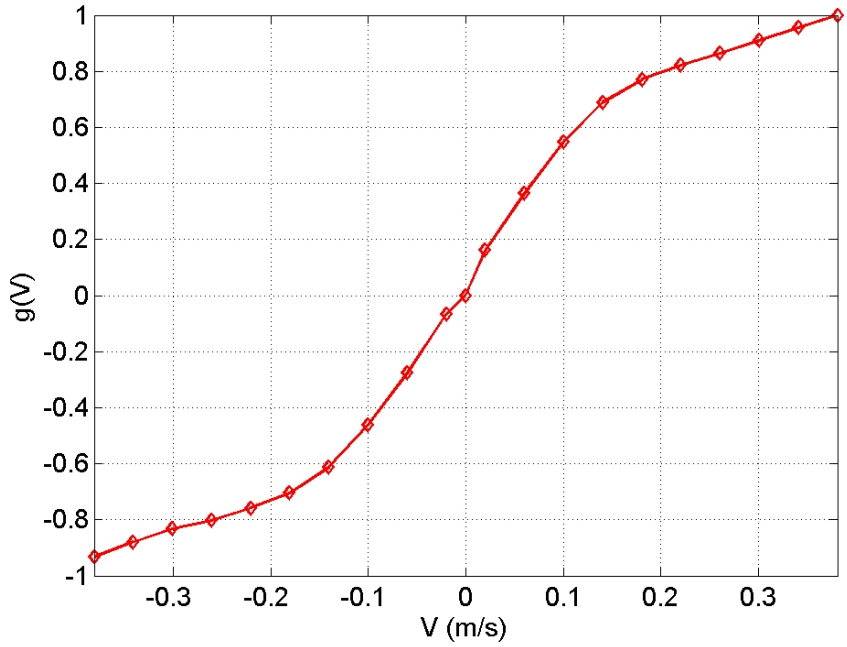

Figure 4.2. Empirically estimated velocity dependent term g(vrel) based on experimental characterization data from Figure 2.1.

The next step in the estimation process is to divide the original MR damper force data $F_{MR}(i, v_{rel})$ by the velocity dependent function $g(v_{rel})$. This scale factor β is given by equation (4.4), and the results of this computation are shown in the plot of Figure 4.1c.

$$\beta(i, v_{rel}) = \left(\frac{F_{MR}(i, v_{rel})}{g(v_{rel})} \right) \tag{4.4}$$

To obtain the current dependent component $f(i)$ we simply average the β scale factor data at each current and across all velocity data.

$$f(i) = \overline{\beta(i)}. \tag{7}$$

Figure 4.3 is a plot of the numerically estimated result for the current dependent term $f(i)$ from equation (2.2). In this particular example, the requirements that $f(0) > 0$ and that $f(i)$ be positive and monotonic are clearly met; however, the estimation method as described above does not guarantee that either condition will be met for every set of damper data. Whereas we can tolerate small deviations from monotonicity in the $g(v_{rel})$ data, the $f(i)$ data must absolutely be monotonic in order for the model inversion process, defined in the following section, to work properly.

In order to confirm that the empirically determined separable functions $f(i)$ and $g(v_{rel})$, as represented by the data in Figures 4.2 and 4.3, match the original characterization data from Figure 2.1, a validation comparison is plotted in Figure 4.4. From this plot, we see that the empirically determined separable model of equation (2.2) is a very reasonable approximation to the experimental damper data.

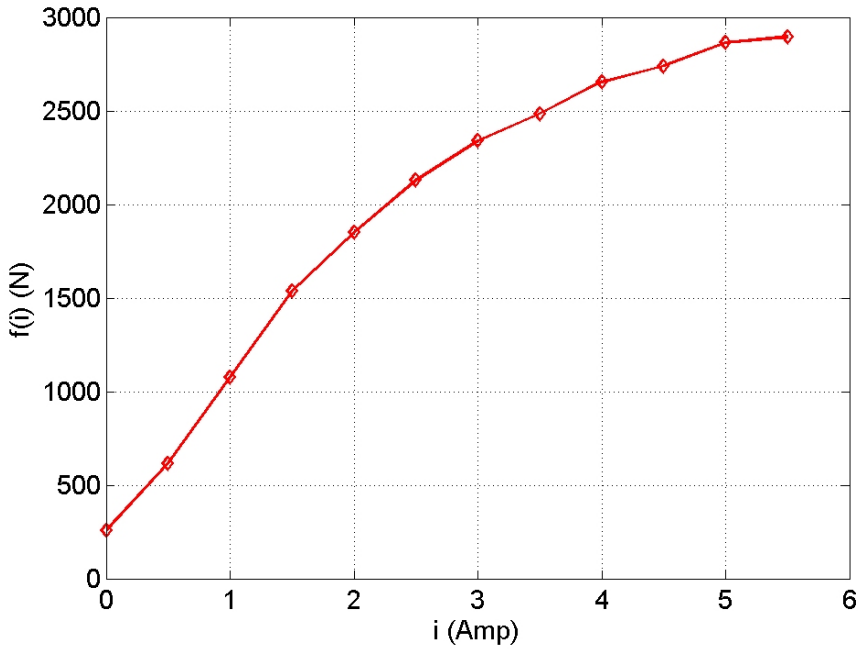

Figure 4.3 Empirically estimated current dependent term f(i) based on experimental characterization data from Figure 2.1. Notice the affine relationship between force and current from 0-5 Amps, but magnetic field saturation effects cause the curve to deviate from linearity with more than 5 Amps.

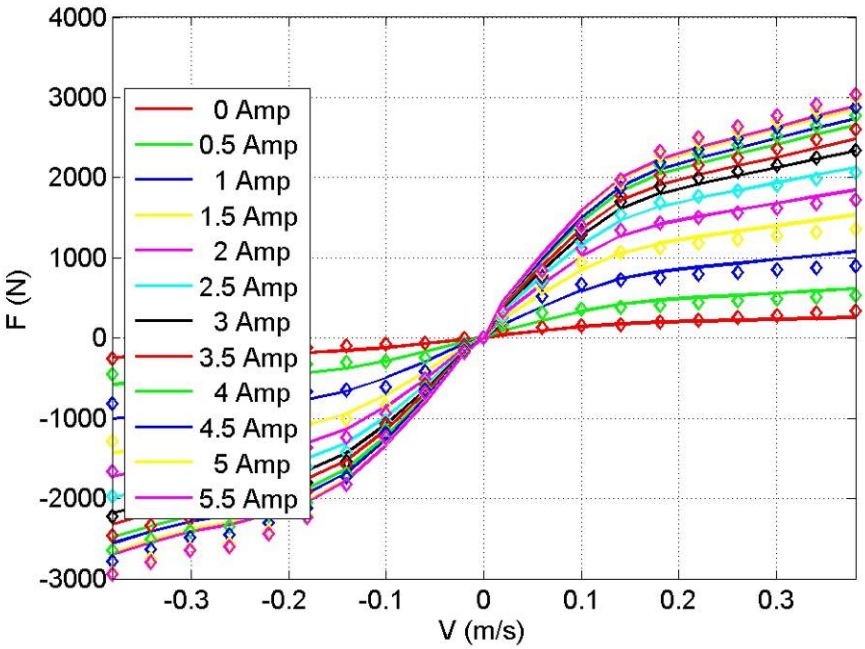

Figure 4.4. Comparison of the original MR damper characterization data with data from the separable model of equation (2.2).

Appendix C provides a more detailed outline for understanding the process presented in this section.

While existing within the category of separable non-parametric models, such as that developed by Song [17], this proposed model accomplishes the same task, but produces a solution with an alternate, non-function based velocity dependence borne directly out of the desire for improved model inversion. As shown in Figure 4.5a, Song represents the force-current relationship with a curve fit, an empirical operation similar to the table look-up used in the proposed model. Velocity however is captured with a hyperbolic function, equation (1.4) and shown in Figure 4.5b. Combination of the two functions results in the model of the damper in Figure 4.6.

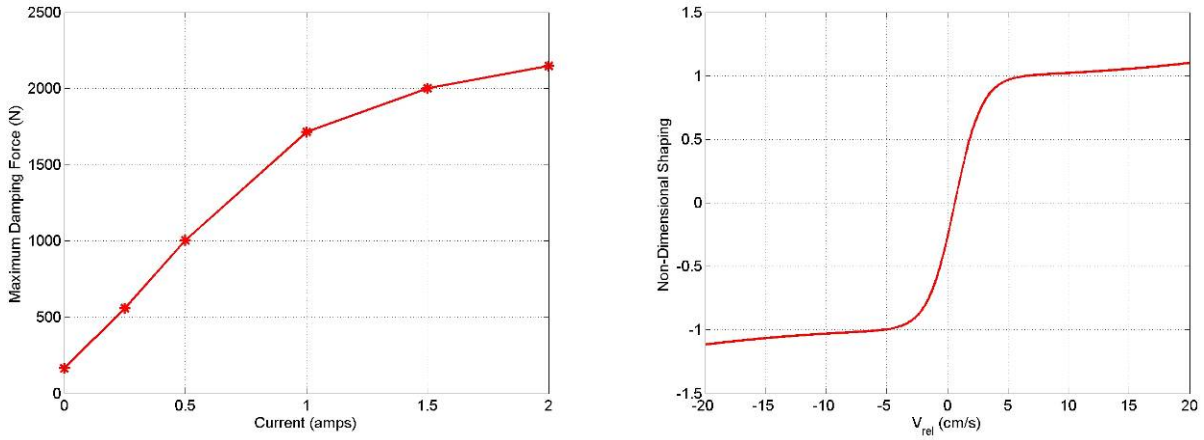

(a) (b)

Figure 4.5. The non-parametric damper model uses the separable functions of current (a) and velocity (b) to generate a representation for damping force capibility.

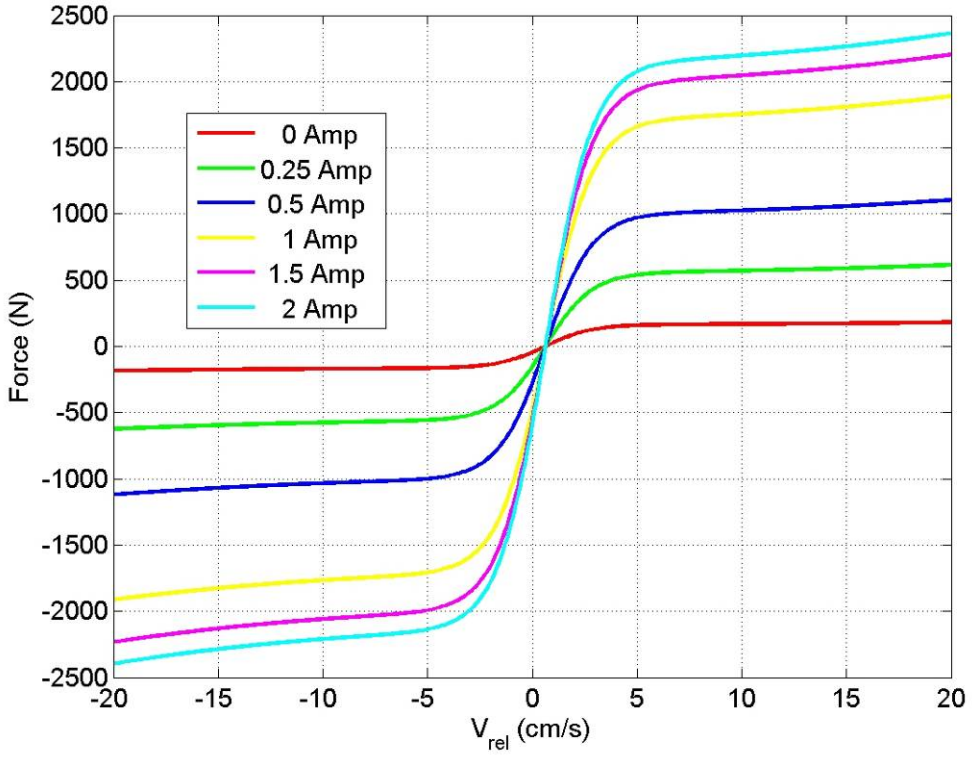

Figure 4.6. Non-Parametric static model resulting from Song's method using data in curves from Figure 4.5.

To illustrate the wide range of applicability, the force-velocity data of the non-parametric model displayed in Figure 4.6 was passed into the new separable model. Results of this exercise indicated that the model was not only able to capture the trends form laboratory characterization data of the MagnaRide damper as shown earlier, but it could also reproduce the results of different models without the need for any tuning parameters. Comparison of Figure 4.7a and Figure 4.5b proves the ability of the new model to automatically adjust for different velocity dependent functions, while comparison of Figure 4.6 and Figure 4.7b show that the modeled forces are identical after manipulation by the separable model.

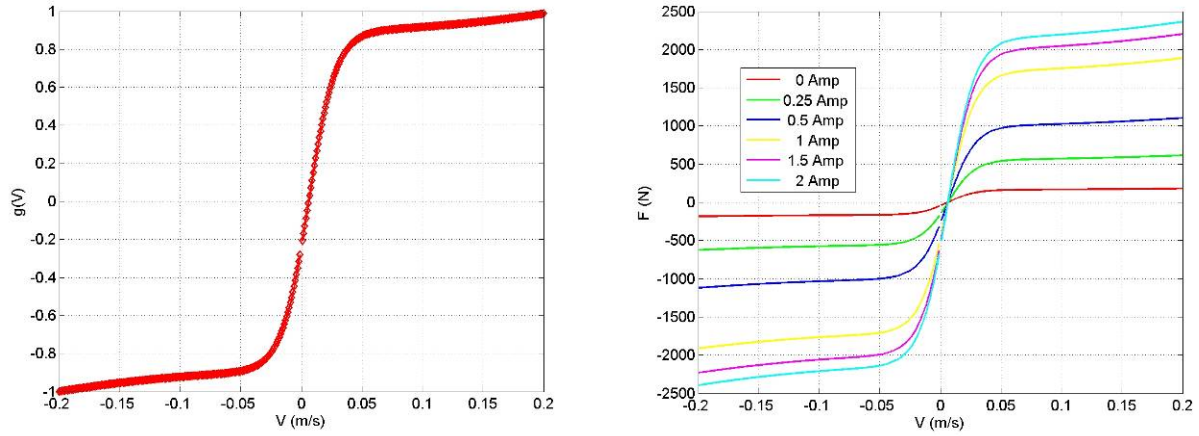

(a) (b)

Figure 4.7. The proposed separable model accurately regenerates the velocity dependence (a) and the static damper model (b).

Chapter 5. Inverse Modeling

5.1: Background

MR dampers are often used in control system development where large forces are required but not a lot of power is available. Common examples include semi-active control systems for primary suspensions [4, 5], seat suspensions [6], and mass dampers for earthquake mitigation in buildings [7]. Many control algorithms are designed with the assumption that the MR damper is a pure force generator while neglecting to explicitly account for the fact that these devices do not create forces that are proportional to the input current [2, 4]. One notable exception is the Skyhook control algorithm, which is explicitly designed to account for the dissipative nature of the MR device [8]. A typical control loop diagram for a primary suspension with an MR damper might look like Figure 5.1.

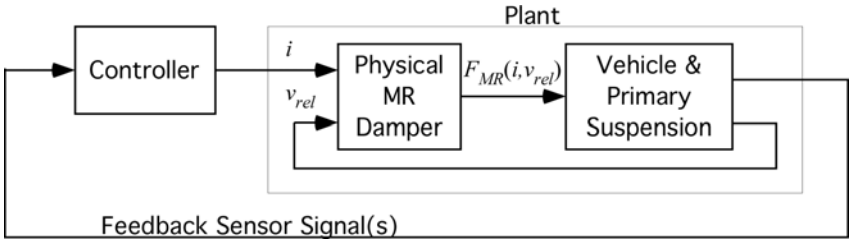

Figure 5.1. Block diagram of generic control loop including an MR damper.

Even the Skyhook control algorithm is designed with the assumption of a commanded force, so when an MR device is employed to create those forces, a disconnect exists between the control algorithm output and the required device input. Any control algorithm that commands a force will require some form of inversion to determine the appropriate command current to produce the desired force in the damper. We can use the simple MR damper model of equation (2.1) to illustrate a common pitfall when designing semi-active control algorithms for MR dampers. If we define $\hat{F}_{MR}$ to be the desired or commanded force from the MR damper, then equation (2.1) indicates that we should choose

$$abs(i) = \frac{1}{\lambda}\left(\frac{\hat{F}_{MR}}{\mathrm{sgn}(v_{rel})}\right) \quad \Rightarrow \quad i = \begin{cases} i_{\max} & \left|\hat{F}_{MR}\right| > \max\left|F_{MR}(i, v_{rel})\right| \\ \lambda^{-1} abs\left(\hat{F}_{MR}\right) & v_{rel} \times \hat{F}_{MR} > 0 \\ 0 & v_{rel} \times \hat{F}_{MR} \le 0 \end{cases}. \tag{5.1}$$

The conditional tests in equation (5.1) reflect the fact that MR devices are dissipative and cannot produce forces in the 2nd and 4th quadrants so the current must be set to zero when those conditions are commanded by the controller. A properly designed semi-active control algorithm will automatically insure that only dissipative forces are commanded. If we ignore the conditional test for the moment, the simple model of equation (5.1) indicates that indeed the current should be proportional to the commanded force. This is the reason why many researchers have been able to show some success without explicitly accounting for the conversion from current to force in the device.

5.2: Inversion of the Separable Model

We assert that any control system design using an MR device will only perform better if an accurate inverse model is employed to convert from commanded force to damper current. Inverting the separable model of equation (2.2) yields

$$i = \begin{cases} i_{\max} & \left|\hat{F}_{MR}\right| > \max\left|F_{MR}(i, v_{rel})\right| \\ f^{-1}\left(\frac{\hat{F}_{MR}}{g(v_{rel})}\right) & \frac{\hat{F}_{MR}}{g(v_{rel})} > 0 \\ 0 & \frac{\hat{F}_{MR}}{g(v_{rel})} \le 0 \end{cases} . \tag{5.2}$$

The proposed separable model will be invertible as long as $f(i)$ is invertible. This will always be true as long as $f(i)$ is strictly monotonic. As in the forward model, the inverse model of $f(i)$ may be implemented as a table lookup, or a polynomial or other curve fit. The result in equation (5.2) is general in that it applies to both fully active and semi-active control laws. Again, a properly designed semi-active control law, such as Skyhook, will insure that only dissipative forces are generated, thus eliminating the need for the $i = 0$ conditional test. Fully active control laws will not generally result in commanded forces that insure dissipation and therefore all conditional tests in equation (5.2) are required. Note also from both equations (5.1) and (5.2), that either approach requires some knowledge of the relative velocity (v_{rel}).

If the simple method is used, either knowingly or unknowingly, errors will necessarily be induced because the actual force delivered will not always match the force commanded by the control algorithm. As indicated in Figure 2.1, the largest errors will occur at smaller velocities. Likewise, we expect that the simple model should be reasonably effective for higher velocity signals. This force error is quantified in the comparison plots of Figure 5.2 below.

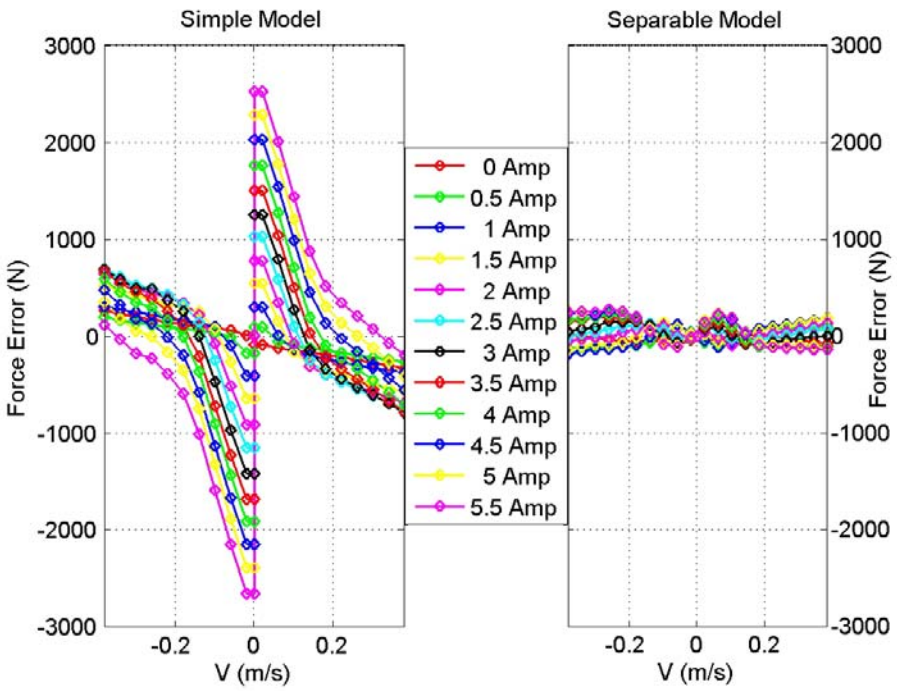

Figure 5.2. Comparison of errors in the commanded force between the simple model of equation (2.1) and the proposed separable model of equation (2.2).

Chapter 6. Hysteresis

6.1: Model Development

To fully incorporate the dynamic effects of the MR damper, the effects of hysteresis must be addressed. Hysteresis in dampers is due to the difference between the accelerating and decelerating paths of the force-velocity curve [15, 25], thus imposing a delay in the changes of internal pressures and ultimately forces.

In terms of mechanical elements, a real damper exhibits hysteresis due to the presence of series compliance in the device. This compliance, the energy storing spring, causes the delays observed in force-velocity plots showing hysteretic behavior. Figure 6.1 provides a graphical description of the damper with series compliance.

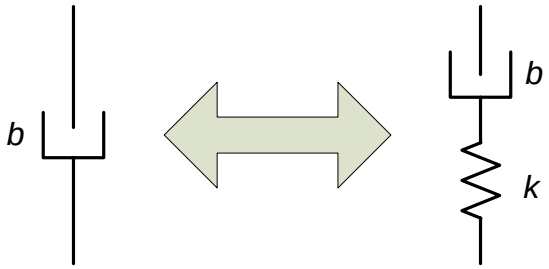

Figure 6.1. Simplified schematic of a damper with series compliance providing hysteresis.

For simplicity, the compliance is modeled as a first order filter [17] with the s-domain representation

$$H(s) = \frac{a}{s+a}, \tag{6.1}$$

which can be transformed for real-time use as a discrete filter using the bi-linear transform

$$s(z) = \left(\frac{2}{T}\right)\left(\frac{z-1}{z+1}\right). \tag{6.2}$$

with sample period T.

Further substitution and simplification leads to the discrete representation of equation (6.4)

$$H(z)=\frac{a}{\frac{2}{T}\left(\frac{z-1}{z+1}\right)+a}=\frac{\overbrace{aT}^{b}(z+1)}{\underbrace{(aT+2)}_{a_0}z+\underbrace{(aT-2)}_{a_1}}=\frac{b\left(1+z^{-1}\right)}{a_0+a_1z^{-1}}, \tag{6.3}$$

$$\begin{aligned} a_0y_k+a_1y_{k-1}&=bx_k+bx_{k-1}\\ y_k&=\underbrace{ba_0^{-1}}_{\alpha}x_k+\underbrace{ba_0^{-1}}_{\alpha}x_{k-1}-\underbrace{a_1a_0^{-1}}_{\beta}y_{k-1},\\ y_k&=\alpha x_k+\alpha x_{k-1}-\beta y_{k-1} \end{aligned} \tag{6.4}$$

This filter is easily placed in series with the force output of the non-hysteretic MR damper model of equation (2.2). The break frequency of this filter is then tuned to a value producing hysteresis similar to that seen in characterization data. For the MagnaRide damper, 50Hz appeared to provide the best estimate throughout the entire range of current.

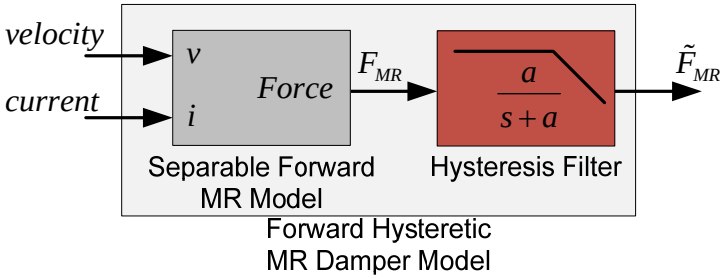

Figure 6.2. Block diagram of forward MR Damper including hysteretic effects.

Application and tuning of this filter resulted in the comparison shown in Figure 6.3. A quick inspection shows that while the modeled hysteresis curves do not match up perfectly with the characterized hysteresis curves for all velocities and currents, the overall trend is nicely captured. This suggests that the approximation of using the first order lag filter in series with the separable forward model is suitable for modeling these effects.

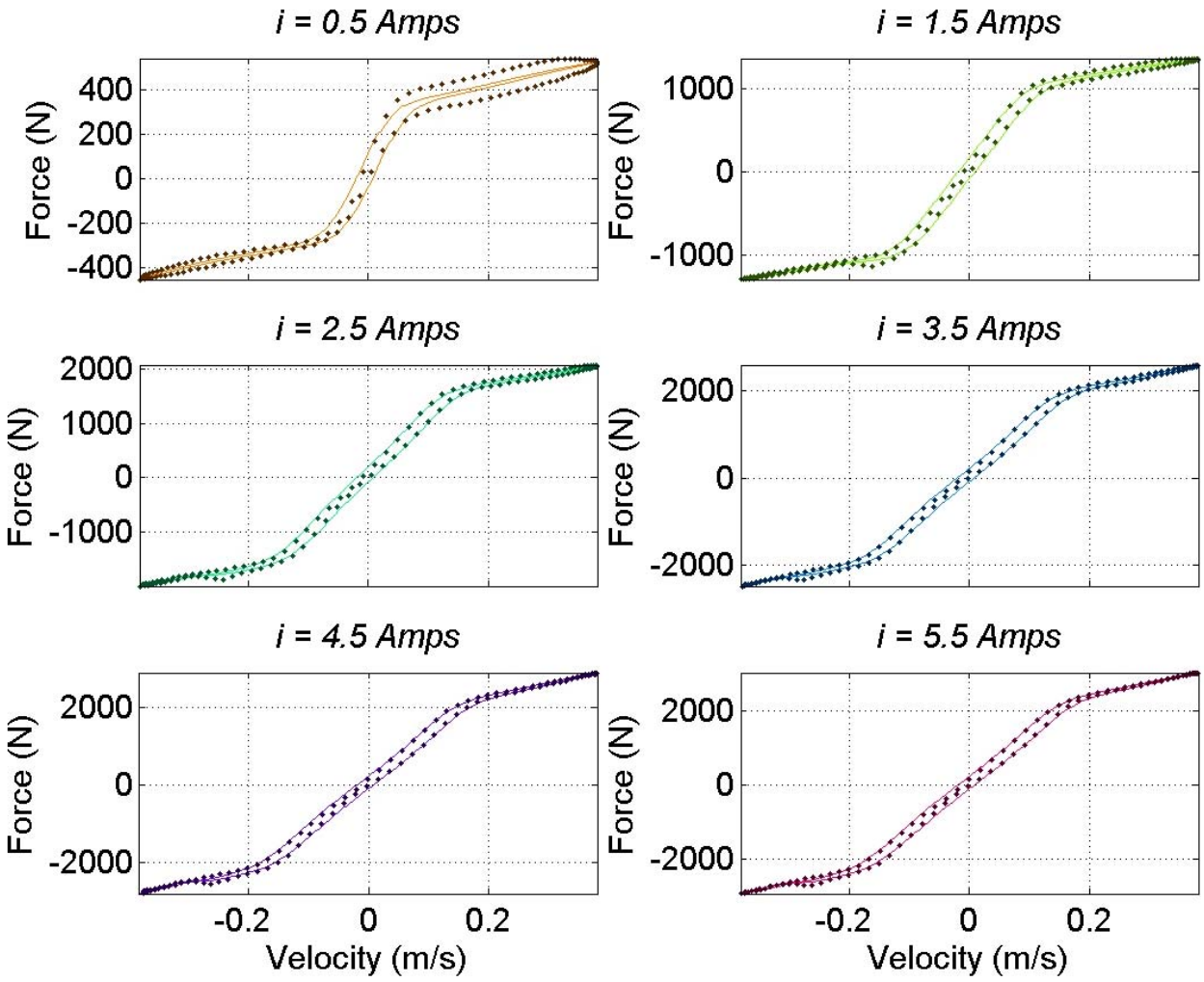

Figure 6.3 Comparison of characterization data hysteresis, shown with "dots", and the modeled hysteresis, shown with solid lines, for a sample of DC currents.

With this addition to the forward model of Chapter 2, the need to develop a generic inverse representation for the hysteresis became clear. It was initially postulated that any tool developed for compensation would need to be applied in the path of the input force of the inverse model. This decision was motivated purely by the observation that, in the same manner of the forward model, the filtering process affected the force path.

In controls literature, the filter shown in equation (6.1) is known as a first order lag [24]. It's opposite is the first order lead compensator.

$$H(s) = \frac{b}{a}\frac{s+a}{s+b}, \tag{6.5}$$

From the simple relationship, it was postulated that the lead compensator could be applied to the force input of the inverse damper model to pre-compensate for hysteretic effects, Figure 6.4.

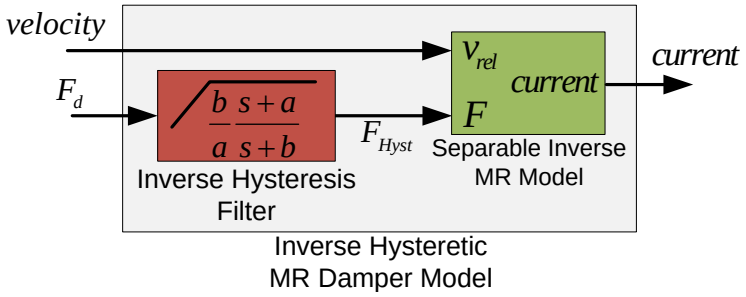

Figure 6.4. Block diagram of Inverse Hysteresis filter with Inverse MR Model.

By cascading the systems from Figures 6.4 and 6.2 to form the system of Figure 6.5, the net effect of the forward and inverse MR models became unity gain. With this simplification, the two filters were analyzed and tuned to a baseline by initially setting the zero of the lead filter to the same frequency as the pole of the lag filter. The pole of the lead filter was then set near half of the sample frequency to make its effects negligible. These settings enforced the system to maintain unity gain at low frequencies and provide a sharp rolloff at high frequency.

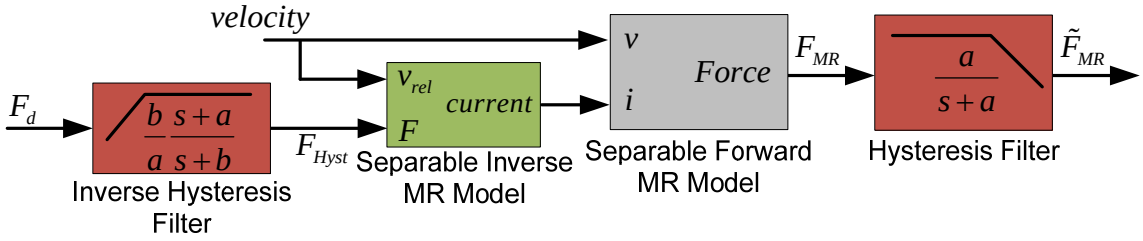

Figure 6.5. Block diagram of the cascaded systems.

6.2: Tuning and Validation

A tuning method was developed such that the zero of the lead filter could be adjusted to reduce force error. This method first excited the forward and inverse models with a sinusoidal velocity. The inverse model, now including the lead filter, also received force command. This force signal assumed that damping was related to the excitation signal by the linear damping coefficient, *b*, in this case *2000 N-s/m*. The inverse hysteretic MR model computed a current related to the inputs which was then passed to the forward hysteretic MR model. The forward model then computed two forces: one including the effects of hysteresis, F_{hyst} and one omitting them, $F_{backbone}$.

Figure 6.6 displays the forces observed during the tuning simulation as well as the command signals. In the first plot, the hysteretic force is shown lagging the non-hysteretic backbone force, but matching up quite nicely to the desired force. The hysteretic force is shown to only have errors at the zero crossing. This error is to be expected as the zero crossings of the force correspond with a maximum absolute acceleration. Due the phase shifts between position, velocity and acceleration, this maximum in acceleration corresponds to an end of damper travel and the unsettled dynamics within the device.

The second plot depicts the command current generated by the inverse model. Current saturation level is also shown. It can be seen that the current saturates when the desired force (proportional to velocity) crosses zero. When velocity reaches zero, the inversion process is faced with a zero-divide condition. This is addressed in equation (5.2) where the inverse model is formulated. To correct for this, the zero velocity is assumed to be machine precision to prevent the simulation from computing an infinite force. The computed force is still quite large however. Large force quantities directly correspond to high current levels as shown by the saturation of current. The final plot describes the same divide-by-zero situation in an intermediate inversion step prior to the delivery of current. It is clear that the desired force is saturated due to the large force ratio.

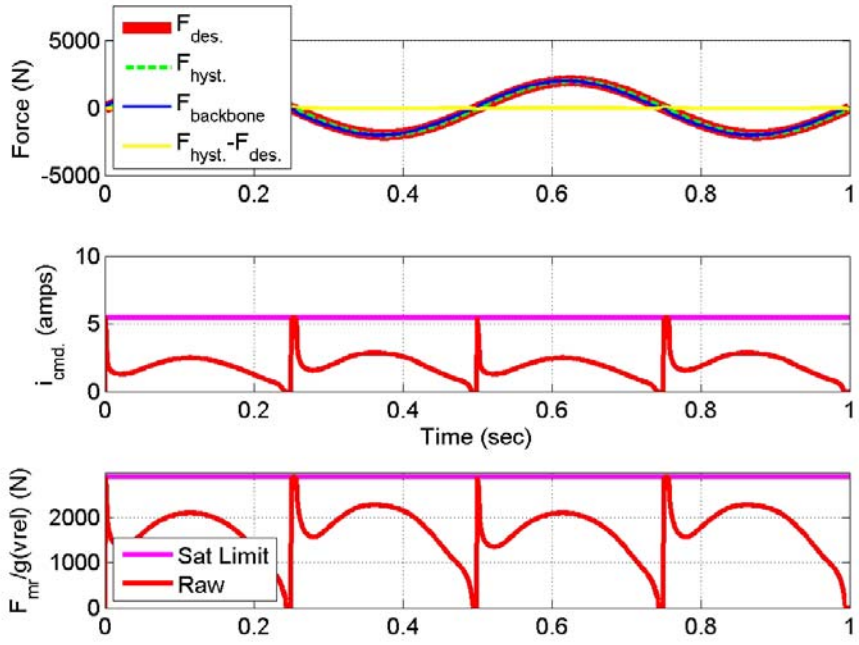

Figure 6.6. Sine wave excitation tuning exercise.

Figure 6.7 provides an alternate depiction of the performance of the system. The lower plot, relative acceleration vs. force error, was primarily used for tuning. The red curve, non-hysteretic force minus hysteretic force, indicates change in the magnitude of the error throughout the acceleration, thus presenting the inherent error due to a lack of lag compensation on the forward model. The green curve, desired force minus hysteretic force, depicts where the overall system, lead and lag filters in place, produces force error. As described earlier, this error is developed at the maximum accelerations where the damper is changing direction.

The upper plot of Figure 6.7 displays the sinusoidal relative velocity compared to three different forces: desired force, hysteretic force and non-hysteretic or *backbone* force. Because of the nature of the linear damper approximation, the desired force is perfectly linear across the velocity range. The *backbone* force deviates from the desired force at all velocities but zero. With the addition of the lag filter to the forward model, the hysteretic force improves upon the *backbone* force and matches the desired force at every speed except zero velocity. These observations correlate with the error displayed in Figure 6.6 and the second plot of Figure 6.7.

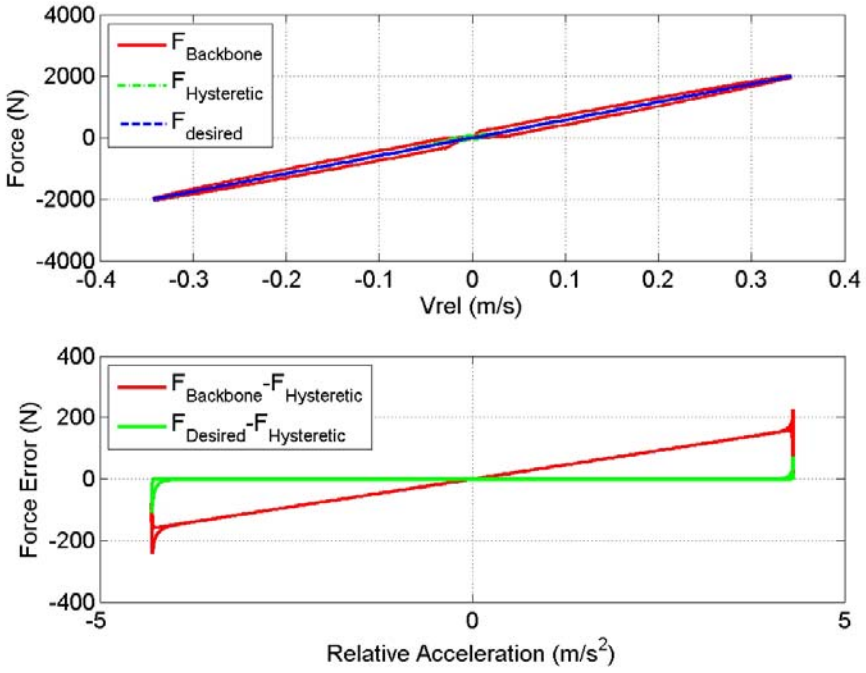

Figure 6.7. Ideal linear damper validation with sine wave excitation.

The desired force minus hysteretic force curve, green in the second plot of Figure 6.7, was used as the primary tuning indicator. The lead filter zero frequency was adjusted until the curve

became zero across acceleration. Upon reaching a satisfactory result in the tuning step of the simulation, the transfer function of the cascaded hysteresis filters could be observed. As shown in Figure 6.8, it was found to be necessary to de-tune the zero of the lead filter from the pole of the lag. Using the assumption that the forward model included a lag with a 50 Hz break frequency and the pole of the lead filter set to 450 Hz, near the Nyquist frequency, tuning of the lead filter's zero to 43.5 Hz produced the best results.

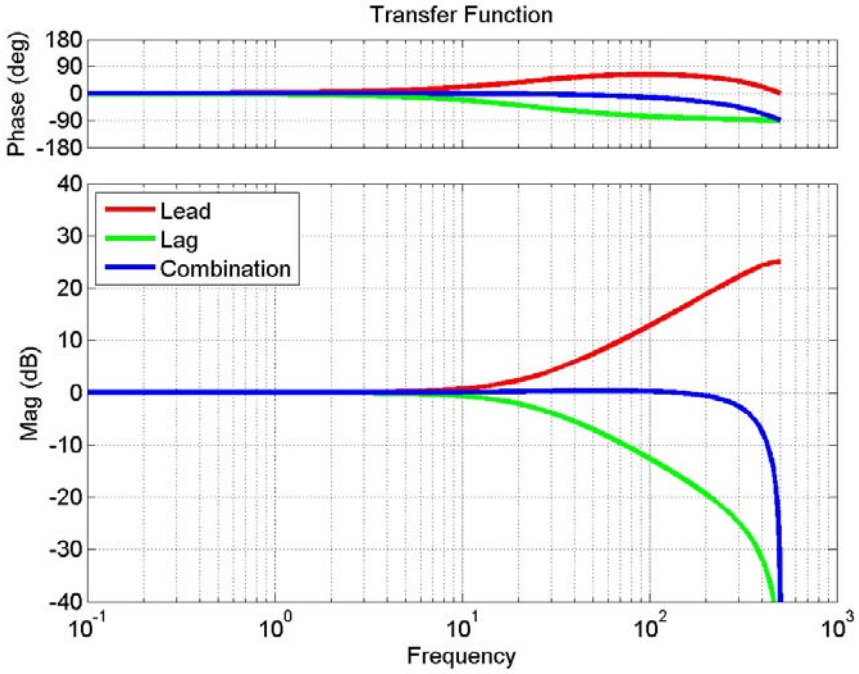

Figure 6.8. Bode diagram of Hysteresis filters and their net effect.

The method for exciting the simulation was then changed to a random signal. The same series of data was collected and plotted. Figure 6.9 shows the time series force, current and intermediate inversion step for the random velocity. The same trends observed in the sinusoidal case carried over to the random case: First, the current spikes occurred at the zero velocity crossings. Next, the *backbone* force lagged the desired and hysteretic forces. And finally, error in hysteretic force only occurred at the zero velocity crossings.

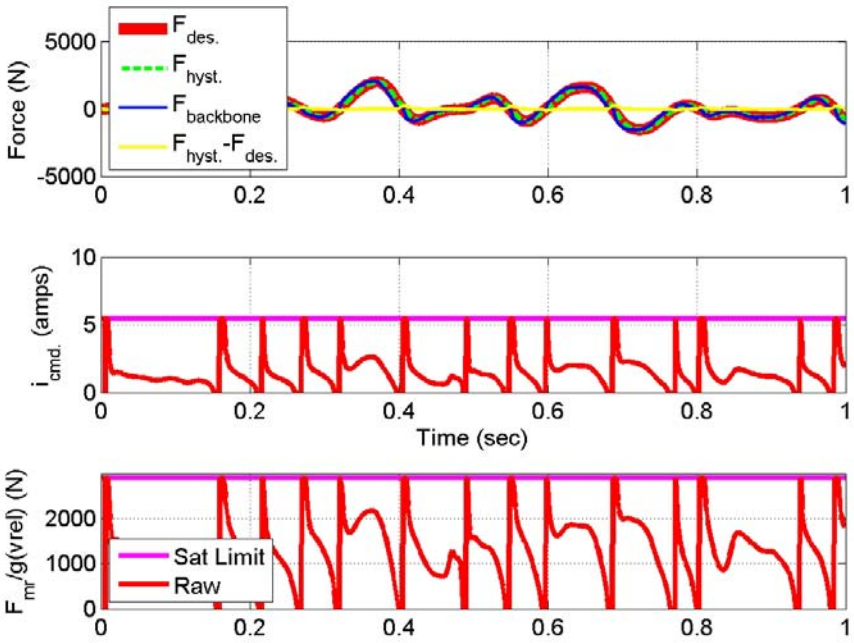

Figure 6.9. Random excitation tuning exercise.

Figure 6.10 describes the same signals as in Figure 6.7. However, the random velocity causes distinct changes in force error of the second plot. The error no longer exclusively occurs at the extreme ends of the relative acceleration range, a trend due purely to a sinusoidal excitation, but now appears each time the direction of travel changes. This is due the lack of periodicity of the input signal and is an expected result. Each time the damper changes direction, force error is produced. Since the damper is changing direction at random, the error is free to occur at each change. In the first plot, the desired force is identical to that of Figure 6.7 as the simulation is trying to achieve a perfectly linear damper. The backbone force has developed more hysteresis due to the random velocity signal. Compensation with the lag filter removes the majority of the hysteresis at high velocities, but does allow some to exist at those velocities near zero due to the zero-divide involved in inversion.

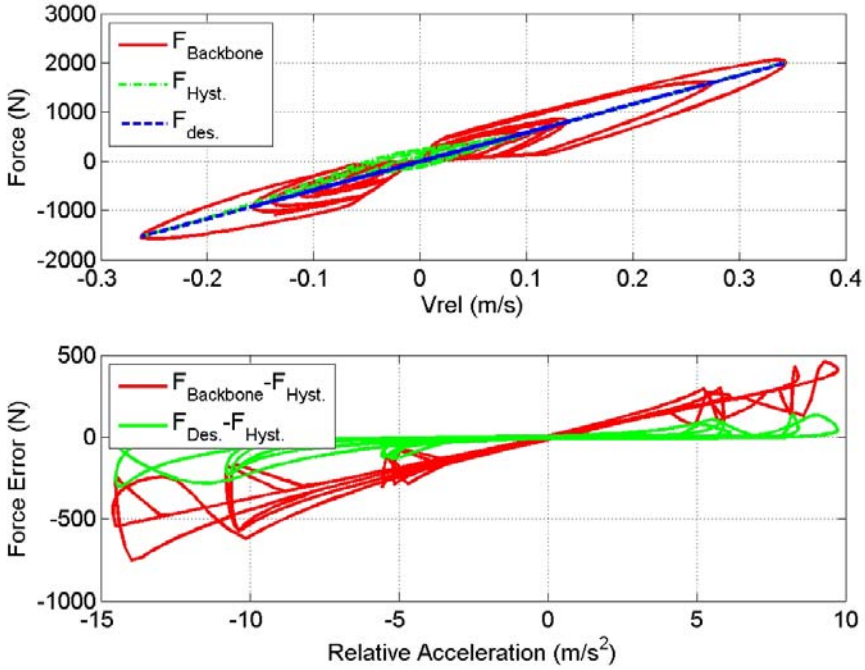

Figure 6.10. Ideal linear damper validation with random excitation.

6.3: Laboratory Validation

Using the MagnaRide MR damper shown in Figure 6.13., the standard characterization process was performed. Results from this characterization are shown in Figure 6.11. Using the processes of Chapters 4 and 5, the *f(i)* and *g(v)* curves were generated and applied to the *Real-Time Hysteretic Inverse MR Model* block of Figure 6.12. This simulation was constructed so that it could be implemented within dSpace for a real-time control simulation.

As in Section 6.2, linear damping behavior was programmed into the *Desired Force Table Look-up* block. A Penny & Gilles potentiometer was fit in parallel with the MagnaRide damper to collect displacement data needed for control. Digital voltage signals corresponding to force from the existing Interface load cell, which is standard equipment on the Roehrig EMA, were accessed and passed into the dSpace environment. Notes in Figure 6.13 indicate each of these instruments. The raw signals were brought into software through dSpace's ADC board. Within the software, a real-time differentiator was used to compute velocity from the displacement data. This differentiator consisted of a complex pole in series with a simple differentiator. Break frequency was set to 5 Hz and damping ratio to 0.3. Velocity was then passed to both the *Desired Force Table Look-up* and *Inverse Hysteretic MR Model*. Desired force computed by the

Desired Force Table Look-up was also supplied to the *Inverse Hysteretic MR Model*. The model, as described in Chapter 5 and section 6.1, computed the necessary current to control damper behavior. This voltage scaled control signal was then passed out of software through the DAC board and converted to a current with a Quanser LCAM linear current amplifier and finally delivered to the MR damper itself. The block diagram of Figure 6.12 describes the signal flow within the dSpace hardware/software.

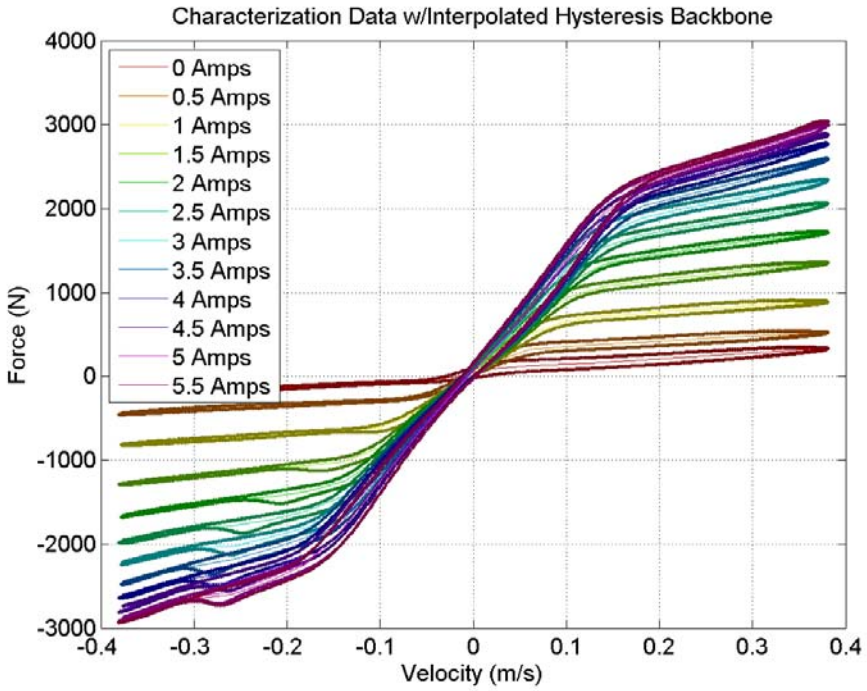

Figure 6.11. MagnaRide Characterization data with backbone.

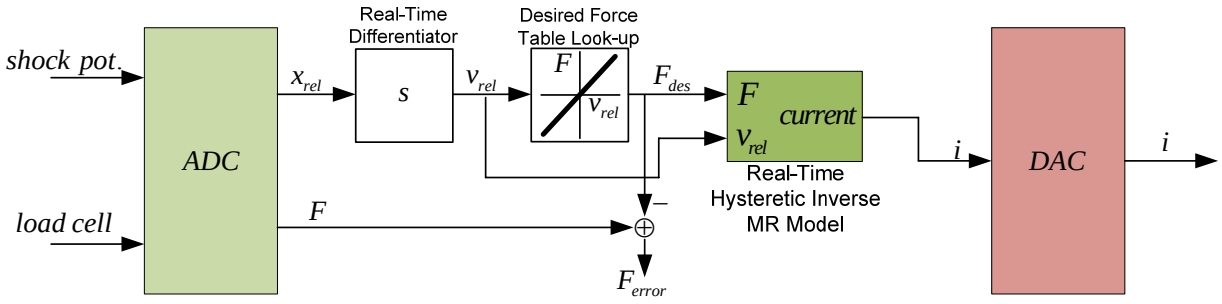

Figure 6.12. Simulink block diagram for dSpace implementation.

With the dSpace software configured, the experiment was run using the methods developed in this thesis and shown in Figure 6.12. First, a sinusoidal excitation was applied to the damper and data was collected. Results of this test are shown in Figure 6.14.

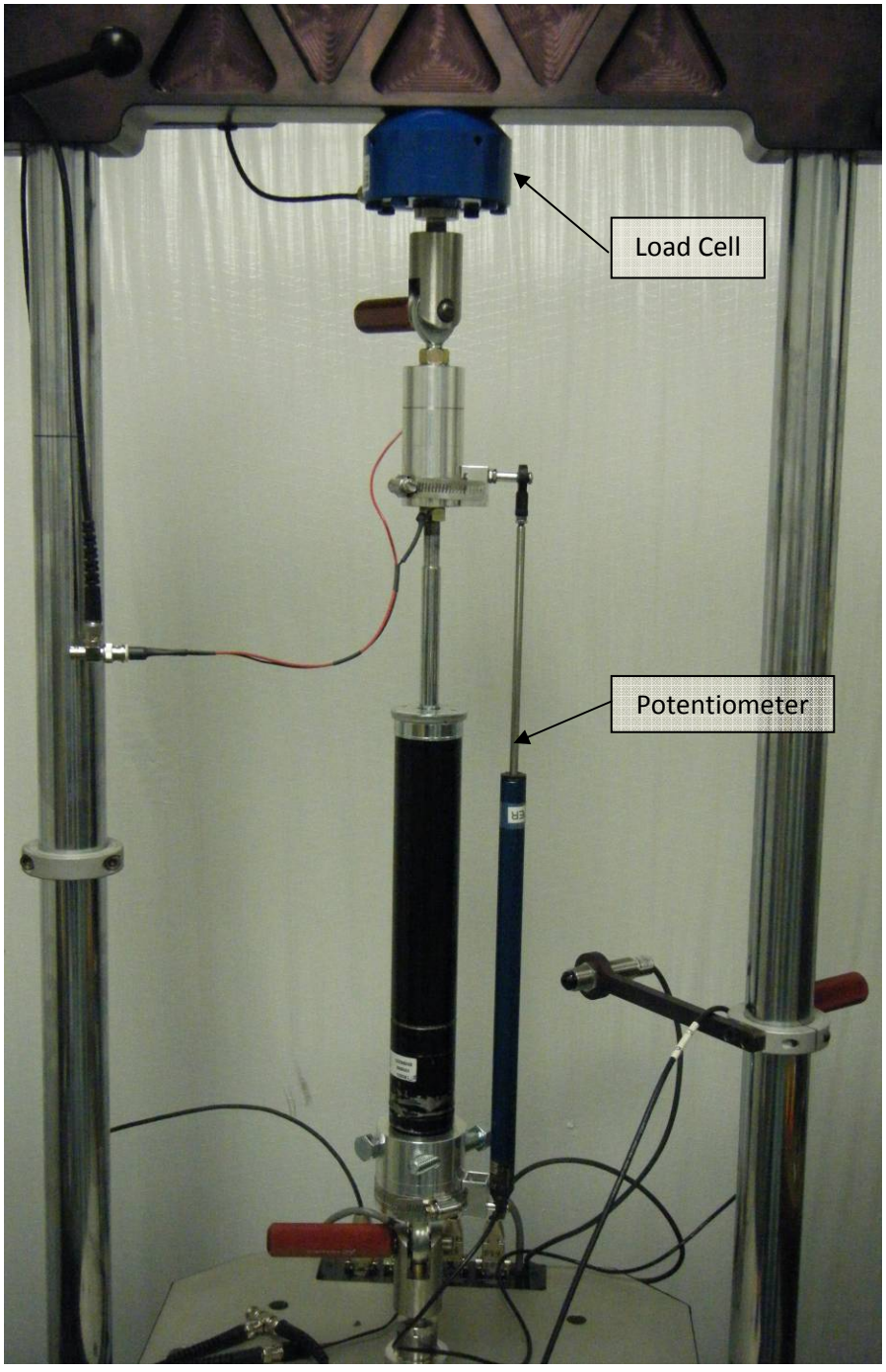

Figure 6.13. Instrumented MagnaRide MR damper on Roehrig EMA Shock Dyno.

Figure 6.14 describes three signals depicting behavior. In the first plot, the time series forces are displayed. Shown in red, the collected force data attempts to mimic the green desired force generated by the linear damper model programmed into the table look-up. The collected force is shown both leading and lagging the desired force depending on what velocity range the damper is operating in. Variations in error caused by the leading and lagging are due to the presence of odd harmonics, specifically the 3rd and 5th, that are not captured by the inverse damper model. Current is shown in the second plot. It is clear that the overall trends of this signal change based on the sign of the velocity. Lack of force symmetry about the x-axis in the characterization of Figure 6.11 directly causes this phenomenon.

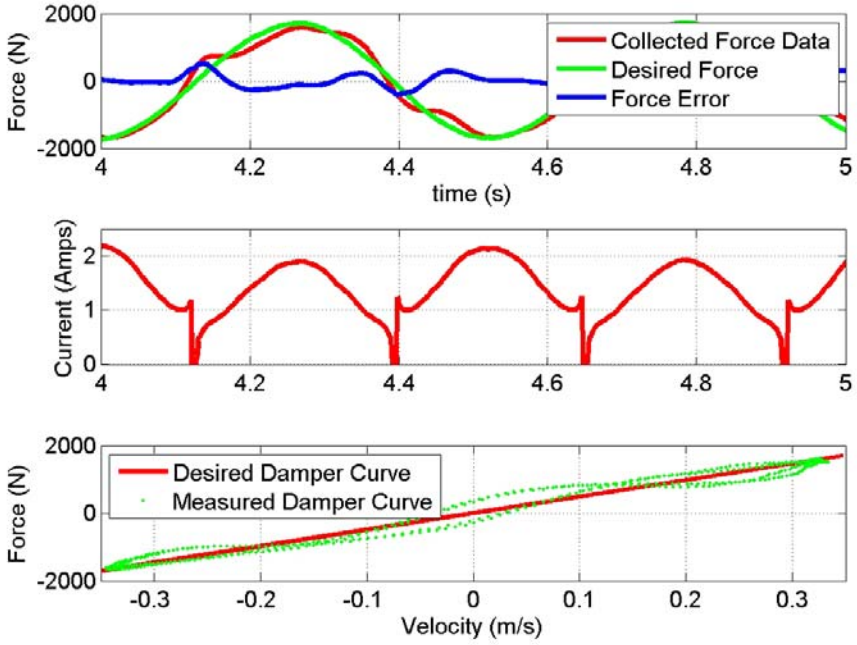

Figure 6.14. Experimentally measured force, supplied current and hysteresis loop for separable inverse MR damper model.

Plotting the force-velocity behavior of the experimental data provided another method to describe the performance of the inverse hysteretic model. Displayed in the third plot, desired damping behavior is shown in red while the measured behavior is shown with green points. Overall, the general trend of the measured data matches the desired behavior nicely. There exists a slope underlying the hysteresis loop suggesting that the controller has effectively bounded the performance of the damper within an adequate margin of error of the desired behavior.

To show the performance gained by implementing the proposed inversion scheme, another experiment was performed. In this experiment, the *hysteretic inverse model* was replaced with the *proportional inverse model*. From analysis of the *f(i)* curve, the optimal conversion parameter for this inversion was set to 520 *N/amps*. The results of this experiment are shown in Figure 6.15.

The first plot shows the collected and desired forces as well as force error similar to that of Figure 6.14. One observation worth noting is that there is almost no phase lead in the collected data. In fact, the collected data generally lags the desired data. Current now adopts a sinusoid-like behavior where the current generated is always the absolute value of the scaled current command.

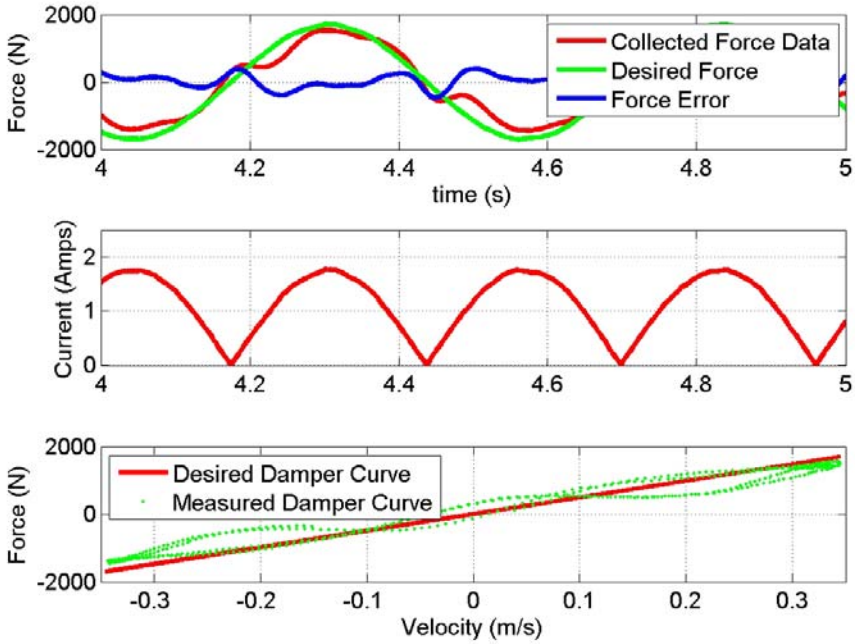

Figure 6.15. Experimentally measured force, supplied current and hysteresis loop for simple inverse MR damper model.

Finally, the last plot describes the force-velocity behavior. Here the same desired damper curve as shown in Figure 6.14 is used. In comparison to the third plot in Figure 6.14, the proportional controller is unable to impose the force to operate within the same margins.

Referring back to first plot if Figure 6.14, the peaks of the forces match up quite nicely suggesting that the inverse model is doing an ample job of matching the needed force

magnitudes. However, there exists a slight ripple in the collected force data that is not present in the desired data. Analysis of the spectrum of this signal indicates the presence of odd harmonics. Figure 6.16 shows this spectrum. Slope changes in the backbone curves excite a square-wave like behavior whenever the inverse controller transitions between these points.

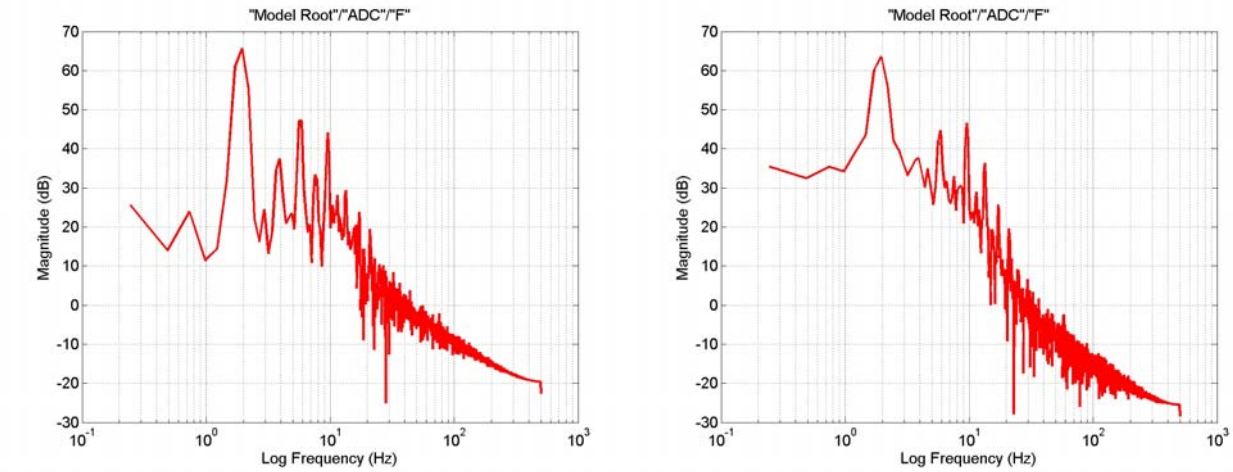

(a) (b)

Figure 6.16. Spectrum of the collected force signals for (a) the separable inversion and (b) the simple inversion.

One final metric for comparing the experimental performance of the proposed controller is shown in Figure 6.17 where force error is plotted against acceleration for both control solutions. Representing the desired acceleration vs. force-error behavior depicted in Figure 6.7, the ideal experimental data would depict elimination of force error along the entire acceleration range not including the small ranges where the damper is changing directions. As opposed to visualizing velocity vs. force-error, this method forced the inherent appearance of zero-crossing errors to appear at the extreme ends of the data instead of showing all of the error stacked around zero velocity. In an un-tuned state, it should first be noted that the lead compensator allowed a constant negative slope throughout the damper's acceleration range.

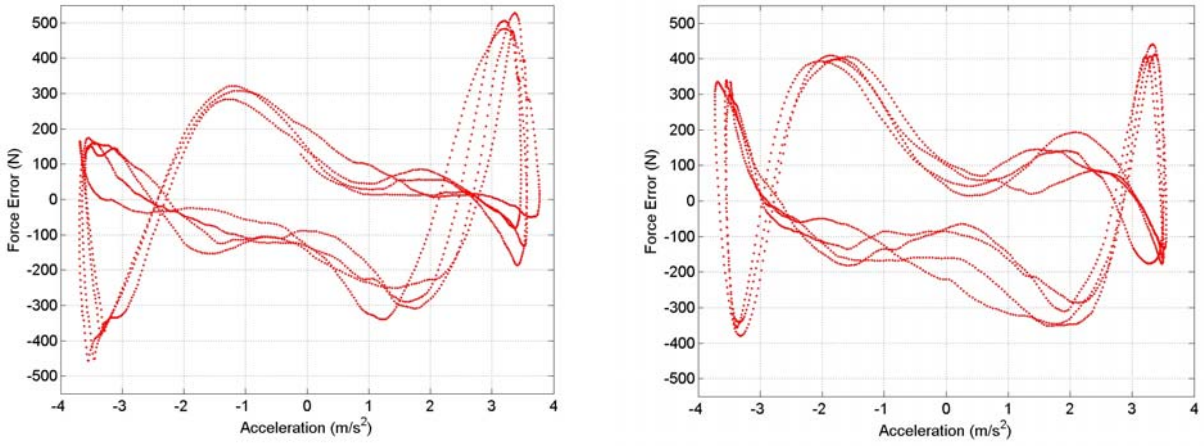

(a) (b)

Figure 6.17. Experimental acceleration versus force error (measured minus desired) for (a) the proposed separable inverse hysteretic model with lead compensation and (b) the simple inverse model.

From Figure 6.17, it can be assumed that, excluding error at the ends of the travel, there exists an average negative slope underlying the error, a trend seen in the tuning exercise. Using separable hysteresis inversion, Figure 6.17a produces a more controlled error than did the proportional inversion of Figure 6.17b. The traces adopted a more linear, parallel, and symmetric trend, all indicators that suggesting the removal of hysteretic effects. This notion adds further evidence for stating the separable inverse model's superiority over the proportional inverse model not only in simulation, but also in the laboratory environment. Further tuning will improve the results presented in Figure 6.17a and eventually allow the error distribution to match that of simulation.

Chapter 7. Proposed Semi-Active Control

To demonstrate the proposed inverse MR damper model augmentation, a simulation study was performed using Matlab and Simulink. The well-known linear two degree-of-freedom quarter car model, Figure 7.1b, was implemented in a state-space formulation, as found in literature [5, 9]. For this study, the semi-active control was incorporated as a pure force generator (F_c) between the sprung (m_s) and unsprung (m_u) masses, where k_s and b_s are the suspension stiffness and damping respectively, and k_t and b_t are the tire stiffness and damping respectively.

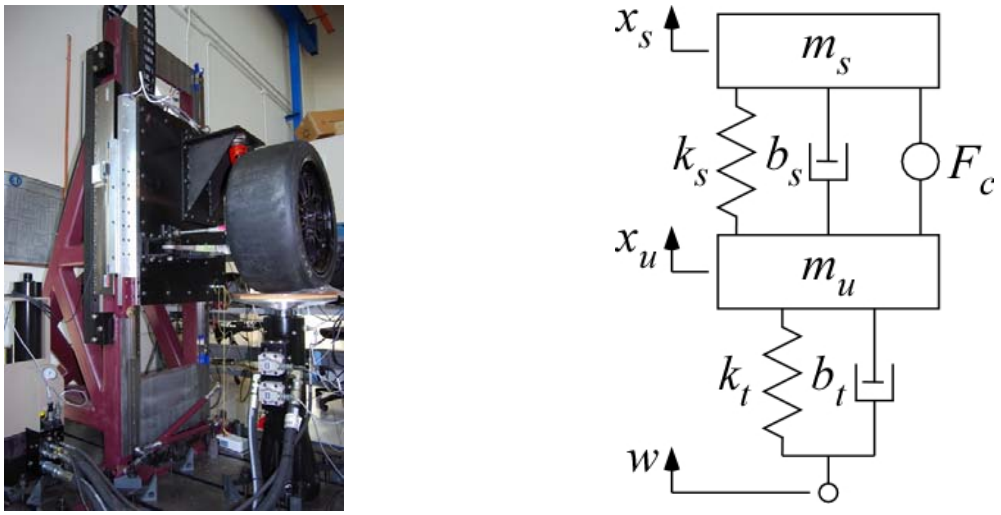

(a) (b)

Figure 7.1. (a) Experimental Quarter-Car test rig which was used to generate the nominal dynamic system parameters, (b) LTI model of Quarter-Car

Figure 7.1b defines the motion of both masses as positive upward. The relative velocity across the suspension is defined as the difference between the sprung and un-sprung mass velocities, $v_{rel} = \dot{x}_s - \dot{x}_u$, which is positive in tension. The absolute velocity is the velocity of the sprung mass $v_{abs} = \dot{x}_s$. Outputs from the state-space model were chosen to be the absolute and relative velocity signals for simplicity.

Table 7.1. Quarter-Car Simulation Parameter Values

Sprung Mass	m_s	250 kg
Un-Sprung Mass	m_u	34 kg
Suspension Damping	b_s	286716 N-s/m
Suspension Stiffness	k_s	423645 N/m
Tire Damping	b_t	5220 N-s/m
Tire Stiffness	k_t	726 N/m

The parameters listed in Table 7.1 were estimated from the experimental setup shown in Figure 7.1a [12]. The estimation process was performed with no physical MR damper in the system; however, the simulation environment allows us to conveniently "turn off" the forces generated from the passive suspension damper and replace it with those from an MR damper, as indicated in Figure 5.1.

In this control study, the classic semi-active Skyhook control law was used [8, 6, 11]. This control law has been predominantly used in semi-active control studies since its inception in the 1970's. The force commanded from the Skyhook control algorithm, equation (7.1), is based on the instantaneous sign of the product of the relative and absolute velocities of the masses shown in Figure 8b.

$$F_D = \begin{cases} -b_{sky} v_{abs} & v_{rel} v_{abs} > 0 \\ 0 & v_{rel} v_{abs} \le 0 \end{cases} \tag{7.1}$$

The wheelpan displacement excitation signal (w) for the simulation was chosen to be a random band-limited noise signal with a peak amplitude of 4mm. The excitation signal, which was constructed by passing white noise through a 1st order low-pass filter at 5 Hz and then through a 4th order low-pass filter at 15 Hz, was used for all subsequent simulations to provide consistency for the comparisons.

Establishing an appropriate Skyhook gain (b_{sky}) is a critical step in tuning the overall system. The gain was selected by means of a baseline simulation comparing two systems in parallel. In the first system, the Skyhook controller directly controls the damping force in the state-space model as if the MR damper were not present, thus representing the "ideal" control case shown in Figure 7.2a. In the second system, an MR damper is incorporated using a separable model, and the inverse MR damper model is used to convert the Skyhook command force to a desired

current as indicated in Figure 7.2b. Both systems simultaneously receive the same excitation, and the Skyhook gain is tuned based on the performance as measured by comparing the outputs. For this simulation, the final Skyhook gain was chosen to have a value of 5000 and the MR damper was numerically sized to deliver up to 3000 N.

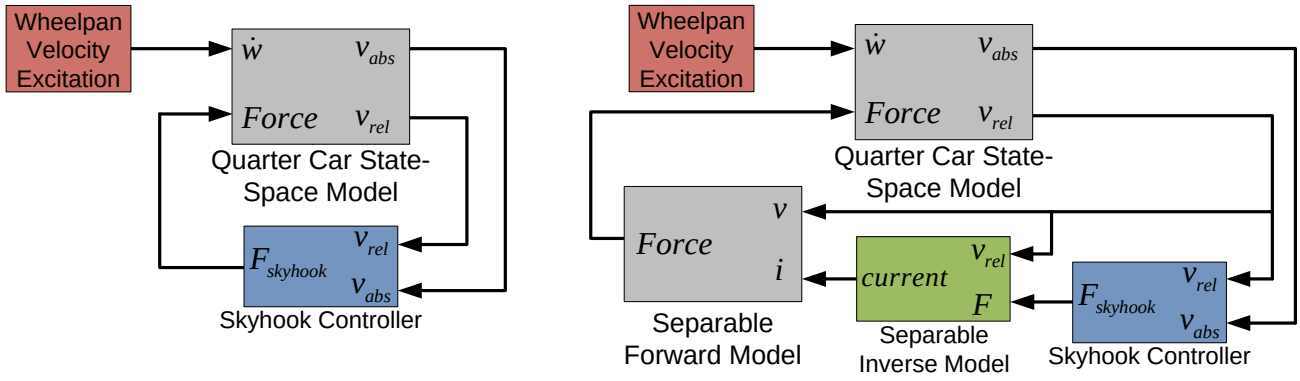

Figure 7.2. (a) Baseline simulation to generate "ideal" Skyhook control force levels, (b) parallel simulation with Semi-Active Skyhook control using an MR damper model and the nonlinear inverse model.

Chapter 8. Simulation Validation

In order to determine whether the nonlinear MR inverse model provides any benefit over the simple model, two control simulations were constructed. In each simulation, the LTI quarter-car state-space model was augmented with the nonlinear separable MR damper model, both shown in Figure 7.2b, to create the quarter-car models indicated in Figure 8.1. Figure 8.1a is the simulation that incorporates the simple inverse model of equation (5.1) very similar to the method proposed in reference [2]. Figure 8.1b is the simulation that incorporates the proposed nonlinear inverse model from equation (5.2) to estimate the appropriate current command that generates the desired command force.

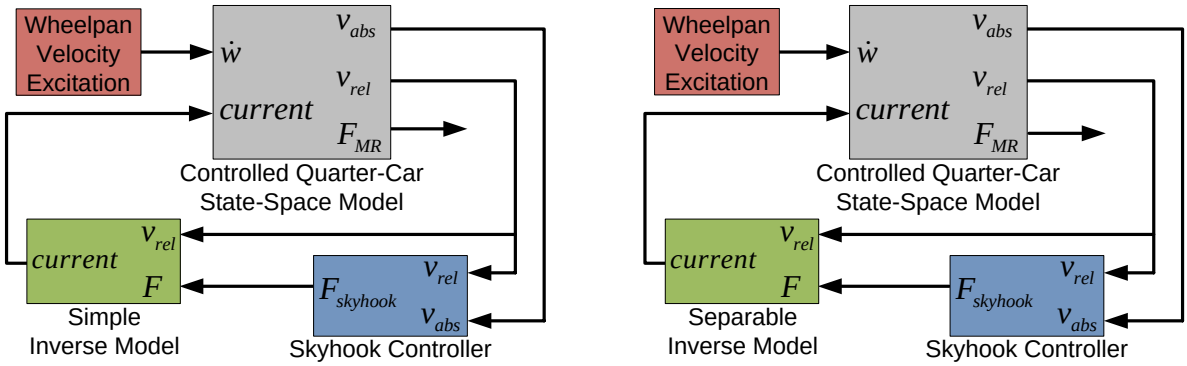

(a) (b)

Figure 8.1. Two parallel simulations were used for comparing the (a) simple inverse model with the (b) nonlinear separable inverse MR damper model.

Simulation conditions governing the comparison study were selected in a manner to ensure a fair comparison of the individual system outputs. In the simulation study, the two parallel systems were excited with the same wheelpan velocity input. Both simulations used the same set of parameter values including the Skyhook gains b_{sky}. By construction, any observable variations in the time responses can only be induced by the effects of the inverse models.

In order to validate the claim that the proposed method provides more benefit for excitations in the low velocity region of an MR damper, simulations were performed at two different input power levels. The first simulation used the excitation as defined in Chapter 7, which is considered here to be the low velocity excitation. For the second simulation, the peak amplitude

of the excitation signal was increased to 9mm and the Skyhook damping gain was re-tuned to a value of 8500. For relative comparison, this second excitation is considered here to be the high velocity excitation.

Both the time response comparisons and the PSD comparisons in Figure 8.2 clearly indicate that the separable model offers some level of improvement over the simple model. This improvement is larger when the MR damper velocity is relatively small where errors in the simple model are the largest compared to the proposed separable model. Figures 4b and 4d also indicate the average power, expressed in decibels, associated with each time response. Figure 4b indicates a 4.25 dB increase in performance with the separable model, whereas Figure 4d indicates only a 0.1 dB increase in performance with the separable model.

Figure 8.3 compares the forces commanded by the Skyhook controller to the forces actually generated by the simulated MR damper. The second plot in Figure 8.3 clearly shows the accuracy improvement in the prediction of MR damper force using the proposed separable model. The first plot in Figure 8.3 indicates that the simple model is trying to apply the correct force, but is significantly limited by the errors as indicated in Figure 5.2.

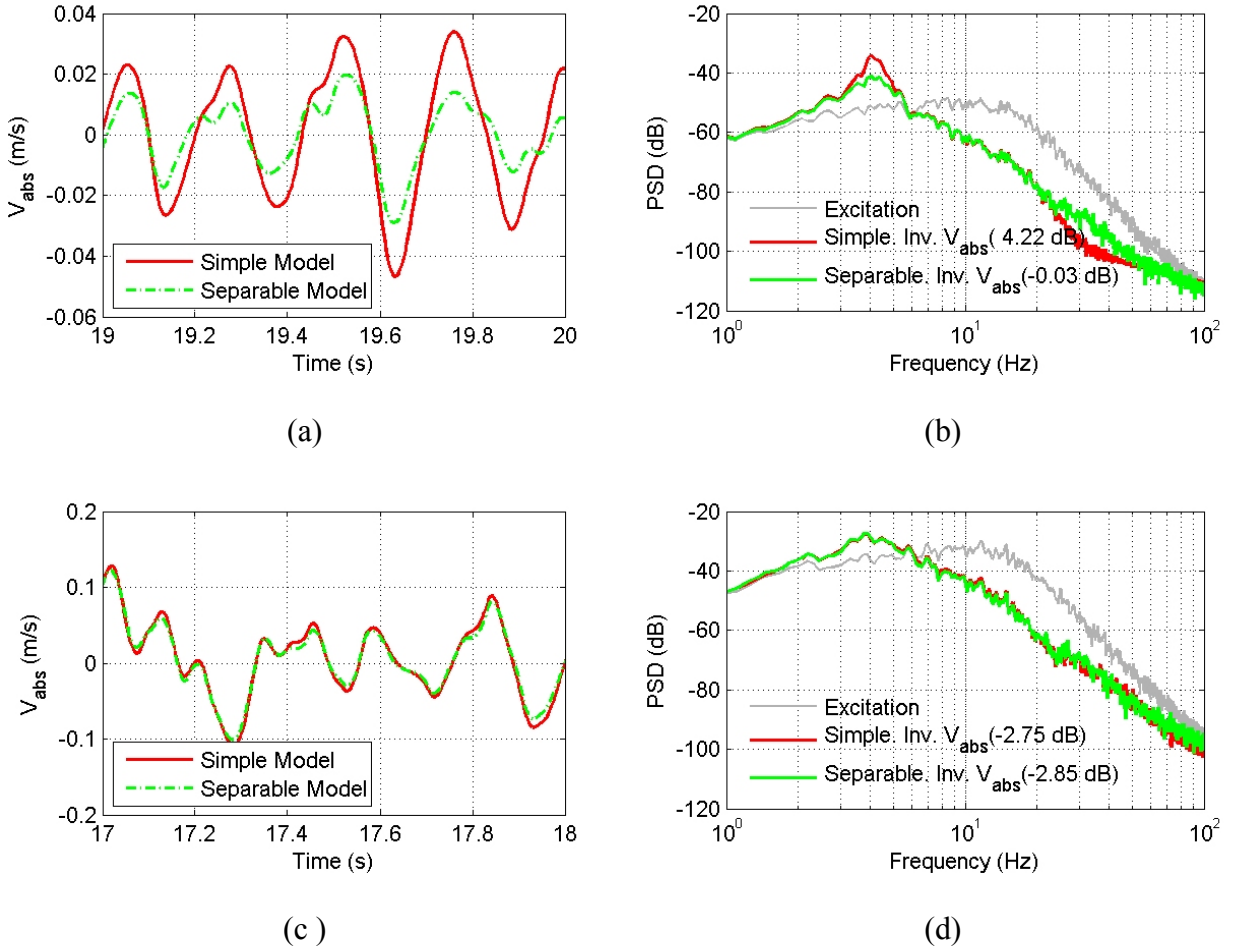

Figure 8.2. Time response comparison indicates that the proposed separable nonlinear inverse model provides significant benefit relative to the simple model for low velocities and only incremental benefit for higher velocities; (a) time response for low velocity excitation, (b) PSD comparison for low velocity excitation, (c) time response for high velocity excitation, (d) PSD comparison for high velocity excitation.

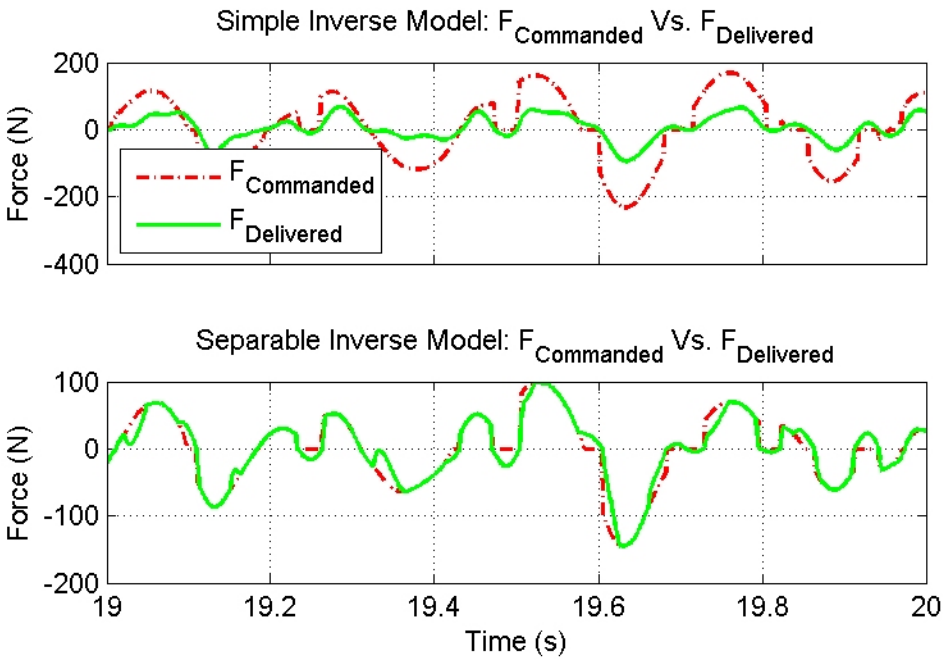

Figure 8.3. Time response of errors between commanded and delivered force.

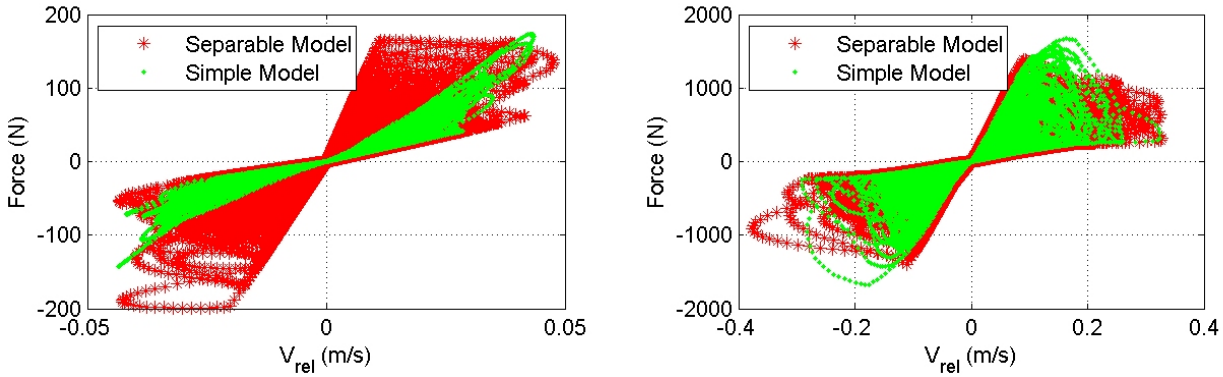

(a) (b)

Figure 8.4. Comparison of the force vs. relative velocity plots for the MR damper resulting from the simple model and the proposed separable model for (a) low velocity excitation and (b) high velocity excitation.

Figure 8.4 shows the force vs. relative velocity curves resulting from the MR damper model in the simulation during the semi-active control process. These plots help to explain the performance results shown in Figure 8.3. When using the proposed separable MR damper model in the control loop, the actual forces generated by the damper cover a larger operating range than what results from using the simple model.

Chapter 9: Conclusions and Recommendations

Conclusions

In this study, a nonlinear model inversion process was developed for improving the performance of semi-active algorithms designed for control systems that use Magneto-Rheological dampers. Simulations on a quarter-vehicle system clearly demonstrate that the proposed control algorithm augmentation has the benefit of significantly enhancing the reproduction of the commanded force. This method requires the existence of a separable inverse model for representing the nonlinear damper characteristics. A method was also proposed and demonstrated for empirically determining an invertible model for an MR damper that is based on experimental data. The proposed nonlinear MR model inversion augmentation may also be used with fully active control algorithms designed with the assumption of a pure force actuation, but are actually operating with semi-active devices.

An alternate method for modeling the MR damper through an adaptive Volterra filter was also presented. While the underlying gradient search method ultimately failed due to the large scale of the solution space, its basic formulation will apply to problems of more linear systems. Investigation into this method also generated a set of constraints that proved useful in the formulation of the separable model.

Inverse hysteretic effects of the damper were postulated to be based on the structure of existing forward hysteretic model assumptions. A method to compensate for these dynamics was proposed and validated through simulation. Results indicated that the method could efficiently compensate for the hysteresis and therefore further increase command force reproduction. Experimental studies were then conducted to further evaluate the benefits of the inverse hysteretic model. A linear damping model was used in a controller to create a target force for the MR damper to produce. These studies showed that the proposed compensation techniques significantly improved the results of "programming" damper behavior within a simple open-loop control algorithm. This was seen in improved linearity of the force-velocity plots and reduction in time-series force-error. Remaining error was analyzed and determined to be due to the presence of odd harmonics.

Recommendations

Further development and validation of the inverted model would include setting up a laboratory experiment on the PERL quarter car rig located in Danville, Va. This would allow for comparison studies between a semi-actively controlled MR dampers and purely passive dampers. Work is currently in progress to install a suspension system on the rig into which the MagnaRide damper can be installed. Improvement in compensation for the hysteretic behaviors is another area for development. However, since this is an open-loop control system, the amount of tunability is hindered when compared to a closed-loop system

References:

[1] Spencer Jr, B.F., et al., "Phenomenological Model for Magnetorheological Dampers," Journal of Engineering Mechanics, **123**(3), p. 230-238, 1997.

[2] Pare, Christopher A., "Experimental Evaluation of Semiactive Magnetorheological Suspensions for Passenger Vehicles," Virginia Tech, MS Thesis, Blacksburg, VA, 1998.

[3] http://www.roehrigengineering.com/

[4] Dixit, R.K. and G.D. Buckner, "Sliding mode observation and control for semiactive vehicle suspensions," Vehicle System Dynamics, **43**(2), p. 83-105, 2005.

[5] Venhovens, P.J.T., "Development and implementation of adaptive semi-active suspension control," Vehicle System Dynamics, **23**(3), p. 211-235, 1994.

[6] Song, X. and Ahmadian, M. 2004. ''Study of Semiactive Adaptive Control Algorithms with Magneto-Rheological Seat Suspension,'' In: 2004 SAE World Congress, Detroit, MI, March 8-11, SAE 2004-01-1648.

[7] Ramallo, J.C., H. Yoshioka, and B.F. Spencer Jr, "A two-step identification technique for semiactive control systems," Structural Control and Health Monitoring, **11**(4), p. 273-289, 2004.

[8] Karnopp, D. C., Crosby, M. J., and Harwood, R. A., "Vibration and Control Using Semi-Active Force Generators," Journal of Engineering for Industry, **96**(2), 619–626, 1974.

[9] Chantranuwathana, S. and P. Huei., "Adaptive robust force control for vehicle active suspensions," International Journal of Adaptive Control and Signal Processing, **18**(2), 83-102, 2004.

[10] Jalili, N., "A Comparative Study and Analysis of Semi-Active Vibration Control Systems," Journal of Vibration and Acoustics, **124**(4), 593-605, 2002.

[11] Ahmadian, M., X. Song, and S.C. Southward, "No-jerk skyhook control methods for semiactive suspensions," Journal of Vibration and Acoustics, **126**(4), 580-583, 2004.

[12] Ziegenmeyer, J., "Estimation of Disturbance Inputs to a Tire Coupled Quarter-Car Suspension Test Rig," Virginia Tech, MS Thesis, Blacksburg, VA, 2007.

[13] Biglarbegian, M., W. Melek, and F. Golnaraghi, "Intelligent Control of Vehicle Semi-Active Suspension Systems for improved Ride Comfort and Road Handling," Proc. NAFIPS, 19-24, 2006.

[14] Snyder, R.A., G. M. Kamath, and N. M. Werely, "Characterization and analysis of magnetorheological damper behavior due to sinusoidal loading," Proc. SPIE 3989, 213, 2000.

[15] Emmons, S., "Characterizing a Racing Damper's Frequency Dependent Behavior with an Emphasis on High Frequency Inputs," Virginia Tech, MS Thesis, Blacksburg, VA, 2007.

[16] Dixon, J. C., 1999, The Shock Absorber Handbook, SAE, Warrendale, PA.

[17] X. Song, M. Ahmadian and S.C. Southward, "Modeling magnetorheological dampers with application of nonparametric approach," *Journal of Intelligent Material Systems and Structures* (2005) (16), pp. 421–432.

[18] Spencer, B. F., Dyke, S. J., Sain, M. K., and Carlson, J. D., "Phenomenological model of a magnetorheological damper," ASCE Journal of Engineering Mechanics, 1996.

[19] Wen, Y. K., "Method of Random Vibration of Hysteretic Systems." Journal of Engineering Mechanics Division, ASCE, Vol. 102, No. EM2, pp. 249–263, 1976.

[20] Gang J., Sain, M. K., Spencer, B. E., Jr., "Nonlinear blackbox modeling of MR-dampers for civil structural control," Control Systems Technology, IEEE Transactions on , vol.13, no.3, pp. 345-355, May 2005

[21] Chan, S.C.K.; Stathaki, T.; Constantinides, A.G., "Adaptive weighted least squares algorithm for Volterra signal modeling," *Circuits and Systems I: Fundamental Theory and Applications, IEEE Transactions on* , vol.47, no.4, pp.545-554, Apr 2000

[22] Widrow, B. and Walach, E., 2008, Adaptive Inverse Control: A Signal Processing Approach, Wiley-IEEE Press, New Jersey.

[23] Widrow, B and Stearns, S., 1985, Adaptive Signal Processing, Prentice-Hall, Inc., New-Jersey.

[24] Nise, N. S., 2003. Control Systems Engineering, 4th Edition, Wiley, New Jersey.

[25] The Öhlins TT44 Manual, 2nd ed., 1999

[26] Zhou, W., Chew, C., Hong, G., "Inverse dynamics control for series damper actuator based on MR fluid damper," Proceedings of the 2005 IEEE/ASME International Conference on Advanced Intelligent Mechatronics, IEEE, pp.473-478, 24-28 July 2005.

[27] Pan, G., Matsuhisa, H., and Honda, Y., "Analytical Model of a Magnetorheological Damper and Its Application to the Vibration Control", in Industrial Electronics Society, 2000. IECON 2000. 26th Annual Conference of the IEEE, pp.1850-1855, 2000.

[28] Goncalves, F., "Dynamic Analysis of Semi-Active Control Techniques for Vehicle Applications," Virginia Tech, MS Thesis, Blacksburg, VA, 2001.

Appendix A: Quarter Car State Space Derivations

Sketching the system and the FBD for the quarter car model:

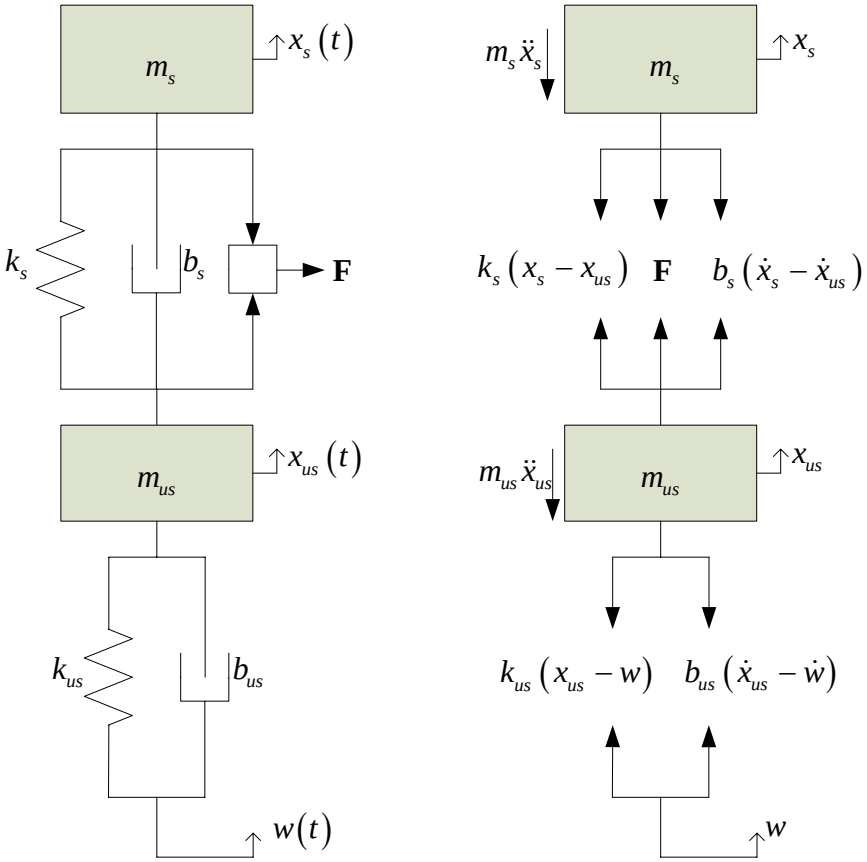

Deriving the equations of motion of the system:

$$m_s\ddot{x}_s + k_s(x_s - x_{us}) + b_s(\dot{x}_s - \dot{x}_{us}) = -F$$
$$m_{us}\ddot{x}_{us} + k_{us}(x_{us} - w) + b_{us}(\dot{x}_{us} - \dot{w}) = F + k_s(x_s - x_{us}) + b_s(\dot{x}_s - \dot{x}_{us})$$

$$m_s\ddot{x}_s + k_s x_s - k_s x_{us} + b_s\dot{x}_s - b_s\dot{x}_{us} + F = 0$$
$$m_{us}\ddot{x}_{us} + k_{us}x_{us} - k_{us}w + b_{us}\dot{x}_{us} - b_{us}\dot{w} - F - k_s x_s + k_s x_{us} - b_s\dot{x}_s + b_s\dot{x}_{us} = 0$$

Defining the state vector:

$$\mathbf{x}(t)=\begin{bmatrix} x_s(t) \\ \dot{x}_s(t) \\ x_{us}(t) \\ \dot{x}_{us}(t) \\ w(t) \end{bmatrix}=\begin{bmatrix} x_1(t) \\ x_2(t) \\ x_3(t) \\ x_4(t) \\ x_5(t) \end{bmatrix}$$

Constructing the state-space realization:

$$\dot{x}_2=\frac{-k_s}{m_s}x_1-\frac{b_s}{m_s}x_2+\frac{k_s}{m_s}x_3+\frac{b_s}{m_s}x_4-\frac{F}{m_s}$$

$$\dot{x}_4=\frac{k_s}{m_{us}}x_1+\frac{b_s}{m_{us}}x_2+\left(-\frac{k_s}{m_{us}}-\frac{k_{us}}{m_{us}}\right)x_3+\left(-\frac{b_s}{m_{us}}-\frac{b_{us}}{m_{us}}\right)x_4+\frac{k_{us}}{m_{us}}x_5+\frac{b_{us}}{m_{us}}\dot{w}+\frac{F}{m_{us}}$$

$$\begin{bmatrix} \dot{x}_s(t) \\ \ddot{x}_s(t) \\ \dot{x}_{us}(t) \\ \ddot{x}_{us}(t) \\ \dot{w}(t) \end{bmatrix}=\underbrace{\begin{bmatrix} \dot{x}_1 \\ \dot{x}_2 \\ \dot{x}_3 \\ \dot{x}_4 \\ \dot{x}_5 \end{bmatrix}}_{\dot{\mathbf{x}}(t)}=\underbrace{\begin{bmatrix} 0 & 1 & 0 & 0 & 0 \\ \frac{-k_s}{m_s} & \frac{-b_s}{m_s} & \frac{k_s}{m_s} & \frac{b_s}{m_s} & 0 \\ 0 & 0 & 0 & 1 & 0 \\ \frac{k_s}{m_{us}} & \frac{b_s}{m_{us}} & \frac{-(k_s+k_{us})}{m_{us}} & \frac{-(b_s+b_{us})}{m_{us}} & \frac{k_{us}}{m_{us}} \\ 0 & 0 & 0 & 0 & 0 \end{bmatrix}}_{\mathbf{A}}\underbrace{\begin{bmatrix} x_1(t) \\ x_2(t) \\ x_3(t) \\ x_4(t) \\ x_5(t) \end{bmatrix}}_{\mathbf{x}(t)}+\underbrace{\begin{bmatrix} 0 & 0 \\ 0 & -\frac{1}{m_s} \\ 0 & 0 \\ \frac{b_{us}}{m_{us}} & \frac{1}{m_{us}} \\ 1 & 0 \end{bmatrix}}_{\mathbf{B}}\underbrace{\begin{bmatrix} \dot{w}(t) \\ F \end{bmatrix}}_{\mathbf{u}(t)}$$

$$\mathbf{y}(t)=\begin{bmatrix} x_s \\ \dot{x}_s \\ x_{us} \\ \dot{x}_{us} \\ w \\ \ddot{x}_s \\ \ddot{x}_{us} \end{bmatrix} = \underbrace{\begin{bmatrix} 1 & 0 & 0 & 0 & 0 \\ 0 & 1 & 0 & 0 & 0 \\ 0 & 0 & 1 & 0 & 0 \\ 0 & 0 & 0 & 1 & 0 \\ 0 & 0 & 0 & 0 & 1 \\ \frac{-k_s}{m_s} & \frac{-b_s}{m_s} & \frac{k_s}{m_s} & \frac{b_s}{m_s} & 0 \\ \frac{k_s}{m_{us}} & \frac{b_s}{m_{us}} & \frac{-(k_s+k_{us})}{m_{us}} & \frac{-(b_s+b_{us})}{m_{us}} & \frac{k_{us}}{m_{us}} \end{bmatrix}}_{\mathbf{C}} \underbrace{\begin{bmatrix} x_1(t) \\ x_2(t) \\ x_3(t) \\ x_4(t) \\ x_5(t) \end{bmatrix}}_{\mathbf{x}(t)} + \underbrace{\begin{bmatrix} 0 & 0 \\ 0 & 0 \\ 0 & 0 \\ 0 & 0 \\ 0 & 0 \\ 0 & -\frac{1}{m_s} \\ \frac{b_{us}}{m_{us}} & \frac{1}{m_{us}} \end{bmatrix}}_{\mathbf{D}} \underbrace{\begin{bmatrix} \dot{w}(t) \\ F \end{bmatrix}}_{\mathbf{u}(t)}$$

Appendix B: Volterra Adaptation Constraints

For an 18 dimensional approximation suggesting 3 coefficients for the current curve fit and 6 coefficients for the velocity shaping curve fit, the constraints are applied as follows:

$$\begin{bmatrix} \begin{pmatrix} v^0 i^0 \\ v^1 i^0 \\ v^2 i^0 \\ v^3 i^0 \\ v^4 i^0 \\ v^5 i^0 \end{pmatrix} \\ \begin{pmatrix} v^0 i^1 \\ v^1 i^1 \\ v^2 i^1 \\ v^3 i^1 \\ v^4 i^1 \\ v^5 i^1 \end{pmatrix} \\ \begin{pmatrix} v^0 i^2 \\ v^1 i^2 \\ v^2 i^2 \\ v^3 i^2 \\ v^4 i^2 \\ v^5 i^2 \end{pmatrix} \end{bmatrix} \Rightarrow \begin{bmatrix} \begin{pmatrix} \beta_0\alpha_0 \\ \beta_1\alpha_0 \\ \beta_2\alpha_0 \\ \beta_3\alpha_0 \\ \beta_4\alpha_0 \\ \beta_5\alpha_0 \end{pmatrix} \\ \begin{pmatrix} \beta_0\alpha_1 \\ \beta_1\alpha_1 \\ \beta_2\alpha_1 \\ \beta_3\alpha_1 \\ \beta_4\alpha_1 \\ \beta_5\alpha_1 \end{pmatrix} \\ \begin{pmatrix} \beta_0\alpha_2 \\ \beta_1\alpha_2 \\ \beta_2\alpha_2 \\ \beta_3\alpha_2 \\ \beta_4\alpha_2 \\ \beta_5\alpha_2 \end{pmatrix} \end{bmatrix}$$

Const.1	*Const*.2	*Const*.3	*Const*.4	*Const*.5
$\alpha_0 = f_0$			$\beta_0 = 0$	
$\alpha_0 = f_0$				$\beta_1 > 0$
$\alpha_0 = f_0$				
$\alpha_0 = f_0$				
$\alpha_0 = f_0$				
$\alpha_0 = f_0$				
	$\alpha_1 > 0$		$\beta_0 = 0$	
	$\alpha_1 > 0$			$\beta_1 > 0$
	$\alpha_1 > 0$			
	$\alpha_1 > 0$			
	$\alpha_1 > 0$			
	$\alpha_1 > 0$			
		$\alpha_2 < 0$	$\beta_0 = 0$	
		$\alpha_2 < 0$		$\beta_1 > 0$
		$\alpha_2 < 0$		
		$\alpha_2 < 0$		
		$\alpha_2 < 0$		
		$\alpha_2 < 0$		

Appendix C: Empirical Modeling Procedure Code

```
function [f, g] = extract_MRdata(F, V, C, C0, debug, saveplot)
%   [f, g] = extract_MRdata(Fmr, Vrel, Current, C0, debug, saveplot)
%
%   Inputs:
%       Fmr = MR Damper Data from the Roehrig Shock Dyno  [Nv x Nc]
%       Vrel = Relative Velocity Data from the Dyno       [Nv x 1]
%       Current = Current levels used in data acq.        [1 x Nc]
%       C0 = nominal current for scaling data to
%       debug = flag to enable debug printing
%       saveplot = flag to save figures as jpeg files
%
%   Outputs:
%       f = estimated current dependent data (force)      [1 x Nc]
%       g = estimated velocity dependent data (non-dim)   [Nv x 1]
%
%   D. Reader    4/5/09

Nc = length(C);      % number of current points
Nv = length(V);      % number of velocity points

if nargin < 4, C0 = C(round(Nc/2)); end
if nargin < 5, debug = 0; end
if nargin < 6, saveplot = 0; end
position = [7,5];
vlim = [min(V),max(V)];  % velocity limits on plot axis

lw = 1.5;             % linewidth for plots

%  --plot the raw force vs. velocity data at each current

if debug,
    figure
    plot(V,F,'-diamond','linewidth',lw)
    grid on
    xlim(vlim)
    legend([num2str(C'),repmat(' Amp',Nc,1)],'Location','Best')
    ylabel('Force (N)')
    xlabel('V (m/s)')

    if saveplot,
        printjpg('raw_F_vs_V.jpg',position)
    end
end

%  --prepare for the extraction processing

Kz = find(abs(V) < eps);    % index for zero velocity data
Knz = find(abs(V) > eps);   % indices for non-zero velocity data

F(Kz,:) = nan*ones(1,Nc);   % NAN out the force data at zero velocity

DC = min(abs(diff(C)));     % the smallest current resolution

K_at_C0 = find(abs(C-C0) < DC);

%  --determine scale factors with respect to the nominal current data

alfa = zeros(size(F));
for i = 1:Nc,
    %  --alfa is a matrix of scale factors at each data point (except V=0)
    alfa(:,i) = F(:,i) ./ F(:,K_at_C0);
end

if debug,
    figure
    plot(V,alfa,'-diamond','linewidth',lw)
    xlim(vlim)
```

```
    grid on
    legend([num2str(C'),repmat(' Amp',Nc,1)],'Location','Best')
    ylabel('\alpha scale factor (non-dim)')
    xlabel('V (m/s)')

    if saveplot,
        printjpg('alfa_vs_V.jpg',position)
    end
end

%  --compute the average scale factor for each current

avg_alfa = mean(alfa(Knz,:));


%  --scale all the force data with the average alfa values at each current

Fsc = zeros(size(F));
for i = 1:Nc,
    Fsc(:,i) = F(:,i) / avg_alfa(i);
end

%  --compute the average scaled force curve

Fave = mean(Fsc')';

if debug,
    figure
    plot(V,Fsc,'-diamond','linewidth',lw)
    hold on
    plot(V,Fave,'w','linewidth',lw)
    grid on
    xlim(vlim)

    legend(str2mat([num2str(C'),repmat(' Amp',Nc,1)],'Average'),'Location','Best')
    ylabel('Average Scaled Force (N)')
    xlabel('V (m/s)')

    if saveplot,
        printjpg('avg_Fscaled_vs_V.jpg',position)
    end
end

%  --compute g by normalizing the average scaled force curve

g = Fave / max(abs(Fave));

g(Kz) = 0;   % reset the zero velocity value: g(0) = 0

if debug,
    figure
    plot(V,g,'-diamond','linewidth',lw)
    grid on
    xlim(vlim)
    ylabel('g(V)')
    xlabel('V (m/s)')

    if saveplot,
        printjpg('g_vs_V.jpg',position)
    end
end

%  --compute f from the average scale factor by dividing g into F

beta = zeros(size(F));
f = zeros(size(C));

for i = 1:Nc,
    beta(:,i) = F(:,i) ./ g;
    f(i) = mean(beta(Knz,i));
end
```

```
if debug,
    %  --scale factor beta
    figure
    plot(V,beta,'-diamond','linewidth',lw)
    grid on
    xlim(vlim)
    legend([num2str(C'),repmat(' Amp',Nc,1)],'Location','Best')
    ylabel('\beta scale factor (N)')
    xlabel('V (m/s)')

    if saveplot,
        printjpg('beta_vs_V.jpg',position)
    end

    %  --f(i) curve
    figure
    plot(C,f,'-diamond','linewidth',lw)
    grid on
    ylabel('f(i) (N)')
    xlabel('i (Amp)')

    if saveplot,
        printjpg('f_vs_C.jpg',position)
    end
end

%  --compare the separable model output to the raw data

if debug,

    Fest = zeros(size(F));
    F(Kz,:) = zeros(1,Nc);

    for i = 1:Nc,
        Fest(:,i) = f(i) * g;
    end

    figure
    plot(V,Fest,'linewidth',lw)
    hold on
    plot(V,F,'diamond','linewidth',lw)
    grid on
    xlim(vlim)
    legend([num2str(C'),repmat(' Amp',Nc,1)],'Location','Best')
    ylabel('F (N)')
    xlabel('V (m/s)')

    if saveplot,
        printjpg('model_validation.jpg',position)
    end
end

%  --compare the simple model output to the raw data

if debug,

    Fmax = max(abs(F(:)))-200;
    Fmin = 0*250;

    lamda = (Fmax-Fmin) / max(C)

    for i = 1:Nc,
        Fest_simple(:,i) = [lamda * abs(C(i)) + Fmin] * sign(V);
    end
    Vs = V;
    k = find(V == 0);
    Vs(k+1,:) = eps;
    Vs(k-1,:) = eps;

    figure
```

```
    plot(Vs,Fest_simple,'linewidth',lw)
    hold on
    plot(V,F,'diamond','linewidth',lw)
    grid on
    xlim(vlim)
    legend([num2str(C'),repmat(' Amp',Nc,1)],'Location','Best')
    ylabel('F (N)')
    xlabel('V (m/s)')

    if saveplot,
        printjpg('simple_validation.jpg',position)
    end
end

%  --compare errors in the simple model and separable model

if debug,

    Esimple = Fest_simple - F;
    Esep = Fest - F;

    k = find(Esimple == 0);
    [m,n] = size(Esimple);

    Esimple1 = [zeros(size(Esimple)) ;zeros(2,n)];
    [o,p] = size(Esimple1);
    Esimple1(1:k,:) = Esimple(1:k,:);
    Esimple1(round(o/2)+1:end,:) = Esimple(k:end,:);

    Esimple1(round(o/2)+1,:) = Esimple(round(m/2)+1,:);
    Esimple1(round(o/2)-1,:) = Esimple(round(m/2)-1,:);

    [m,n] = size(V);
    Vs1 = [zeros(size(V)) ;zeros(2,n)];
    [o,p] = size(Vs1);
    Vs1(1:k,:) = V(1:k,:);
    Vs1(round(o/2)+1:end,:) = V(k:end,:);

    Vs1(round(o/2),:) = eps;
    Vs1(round(o/2),:) = eps;

    figure
    subplot(1,2,1)
    plot(Vs1,Esimple1,'-diamond','linewidth',lw)
    grid on
    xlim(vlim)
    ylabel('Force Error (N)')
    xlabel('V (m/s)')
    title('Simple Model')
    yl = ylim;

    subplot(1,2,2)
    plot(V,Esep,'-diamond','linewidth',lw)
    grid on
    xlim(vlim)
    legend([num2str(C'),repmat(' Amp',Nc,1)],'Location','Best')
    legend('ResizeLegend')
    ylabel('Force Error (N)')
    xlabel('V (m/s)')
    title('Separable Model')
    ylim(yl)

    if saveplot,
        printjpg('error_plot.jpg',position)
    end
end

return
```